Journal of
Manufacturing and Materials Processing

MDPI

Review

Fundamentals of Cooling Rate and Its Thermodynamic Interactions in Material Extrusion

Ahmad Saeed Alzahrani [1,2], Muhammad Khan [1,*] and Feiyang He [1]

[1] Faculty of Engineering and Applied Sciences, Cranfield University, Bedfordshire MK43 0AL, UK; ahmad.alzahrani@cranfield.ac.uk or asm.alzahrani@bu.edu.sa (A.S.A.); feiyang.he@cranfield.ac.uk (F.H.)
[2] Mechanical Engineering Department, Faculty of Engineering, Al-Baha University, Alaqiq 65779-7738, Saudi Arabia
* Correspondence: muhammad.a.khan@cranfield.ac.uk; Tel.: +44-(0)1-2347-54788

Abstract

Material Extrusion (ME) is a layer-by-layer additive manufacturing technique that has gained prominence due to its simplicity, cost-effectiveness, design freedom, and adaptability to a wide range of thermoplastic materials. However, the mechanical performance of ME-printed parts often remains suboptimal, primarily due to complex thermal phenomena that govern microstructural development during the printing process, which are key determinants of mechanical strength. As a result, optimizing thermodynamic printing parameters has become essential for improving the overall quality of the printed parts. Extensive research articles and reviews have been published to explore the effect of many ME printing parameter settings on the resultant product characteristics. Despite this focus, the effect of cooling rate, a critical thermodynamic parameter of the process, has been largely overlooked in current research when they are critically reviewed. Cooling rate plays a central role in determining the thermal history of printed material, which in turn influences polymer chain mobility and microstructural features of the extruded material, all of which are crucial to the mechanical integrity of the printed part. Thus, it has been concluded by this review that analytical and empirical investigations into the influence of cooling rate on the microstructural properties of ME parts represent a valuable and novel contribution to the academic field.

Keywords: additive manufacturing; cooling rate; fused deposition modelling; material extrusion; microstructural properties; printing parameters

check for updates

Academic Editor: Guido Di Bella

Received: 6 November 2025
Revised: 5 December 2025
Accepted: 10 December 2025
Published: 16 December 2025

Citation: Alzahrani, A.S.; Khan, M.; He, F. Fundamentals of Cooling Rate and Its Thermodynamic Interactions in Material Extrusion. *J. Manuf. Mater. Process.* **2025**, *9*, 412. https://doi.org/10.3390/jmmp9120412

Copyright: © 2025 by the authors. Licensee MDPI, Basel, Switzerland. This article is an open access article distributed under the terms and conditions of the Creative Commons Attribution (CC BY) license (https://creativecommons.org/licenses/by/4.0/).

1. Introduction

Additive Manufacturing (AM), commonly referred to as 3D printing, has gained prominence for its ability to produce complex and customized geometries while minimizing material waste compared to conventional methods [1]. According to ASTM and ISO standards, AM processes are classified into seven categories: vat photopolymerization, powder bed fusion, material extrusion, binder jetting, sheet lamination, directed energy deposition, and material jetting [2]. Among these, material extrusion (ME), typically referred to as Fused Deposition Modelling (FDM) or Fused Filament Fabrication (FFF), is the most widely used for polymeric applications. Its adoption spans biomedical scaffolds, aerospace tooling, prototyping, and many other applications, as shown in Figure 1 [2–9].

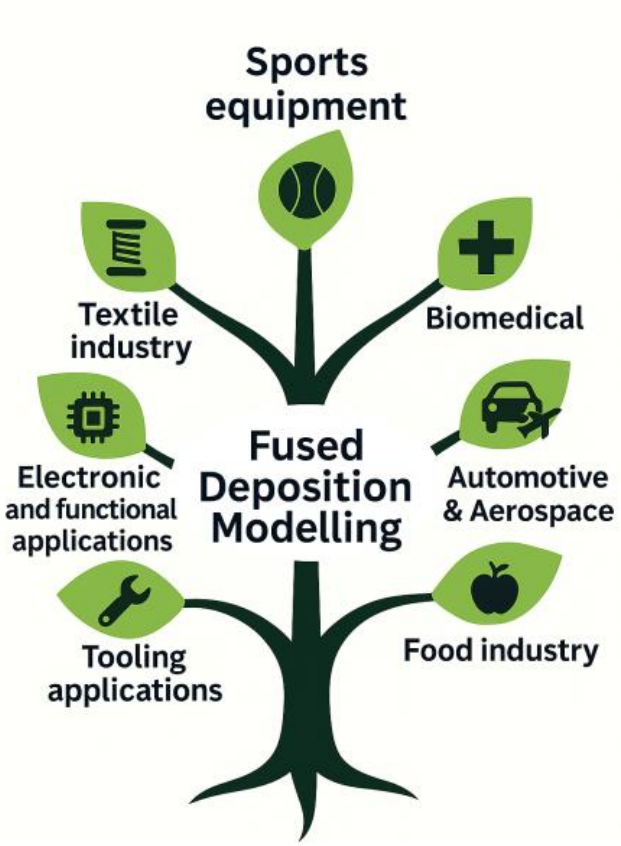


Figure 1. FDM applications in industries [3].

ME operates by heating a thermoplastic filament, extruding it through a nozzle, and depositing it layer by layer onto a build platform, where it rapidly solidifies upon cooling [3–15]. Figure 2 introduces a schematic for both the ME process and ME printer parts. However, mechanical anisotropy, porosity, and weak interlayer adhesion remain limitations due to the thermal history of deposited material [9,10,12–14].

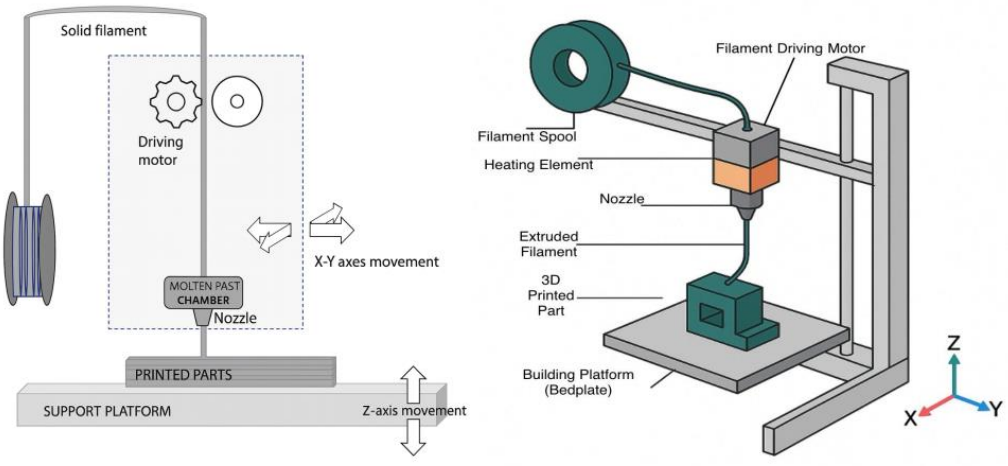


Figure 2. On the left, Schematic for FDM Process [10]; On the right, Parts of FDM Printer [14].

ME provides extensive control over the printing process parameters. Numerous parameters significantly influence the characteristics of the constructed components and their overall quality, as Figure 3 shows [16]. Therefore, effective control of the FDM process is key for enhancing print quality, reducing failures, and maximizing the mechanical properties of printed parts [17–22]. Although the complexity of the relation between

controlling these parameters and the resultant mechanical properties, this relation has been extensively to fairly explored in numerous scholarly articles and reviews [7]. However, when reviewing these studies critically, it has been found one critical exception: the cooling rate. A comprehensive effort is still required to emphasize the cooling rate's influence on the quality of the result of the process.

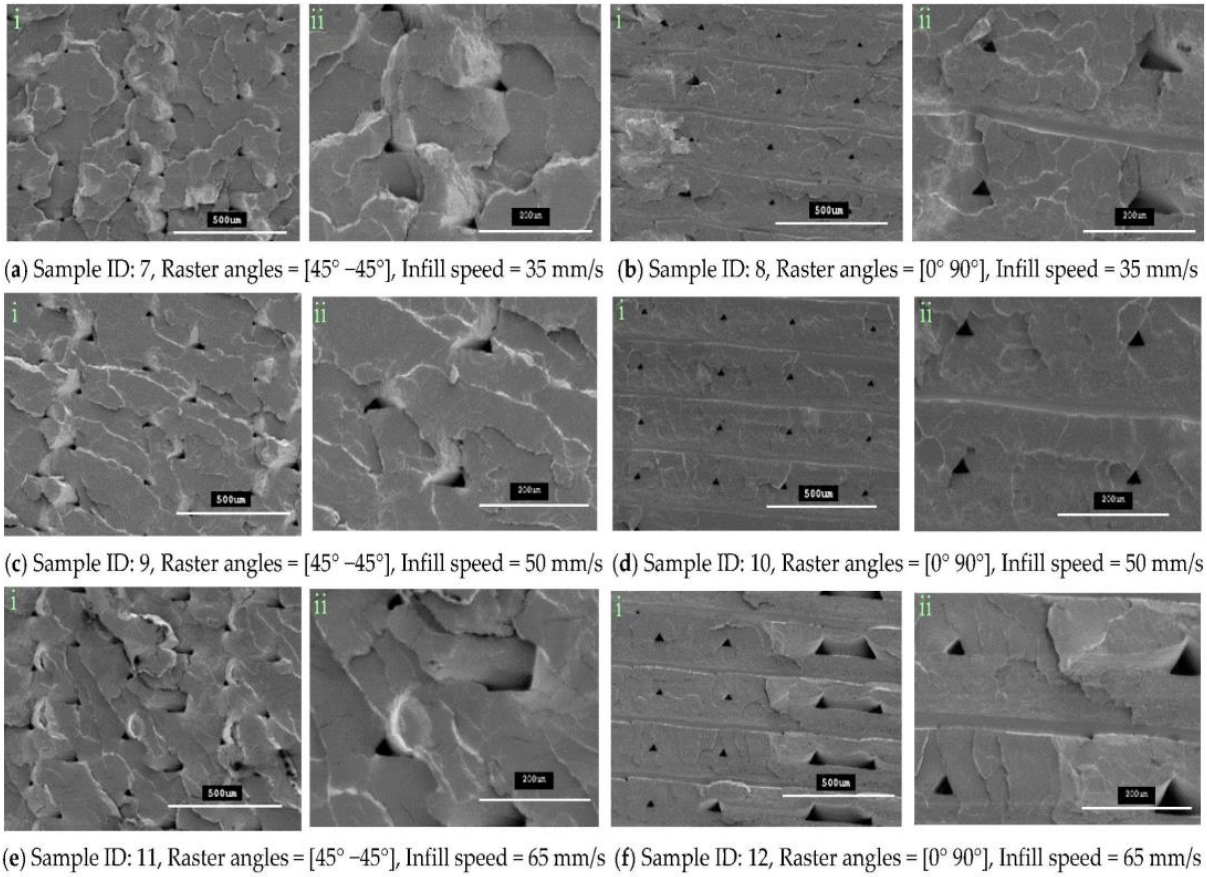


Figure 3. SEM micrographs of tensile-fractured specimens printed at different raster angles and infill speeds. Panels (**i**) were imaged at ~500× magnification (scale bar = 500 µm), and panels (**ii**) at ~800× magnification (scale bar = 200 µm) [19].

Unlike independent process parameters, cooling rate is a derived thermodynamic parameter influenced by nozzle and bed temperatures, printing speed, and structural design choices [11]. It governs crystallinity, bonding quality, and residual stress distribution [22].

This review emphasizes cooling rate as the unifying factor linking ME parameters with microstructural and mechanical properties, providing a thermodynamic framework for process optimization.

To facilitate a coherent reading of the paper, the review is structured to progress from foundational principles to applied insights. It begins by outlining the core thermodynamic and heat-transfer principles governing cooling behaviour in material extrusion. The discussion then examines how cooling rate influences microstructure, crystallinity, defect formation, and interlayer bonding. Building on this foundation, the review consolidates findings from previous optimization studies within a cooling-rate-centred framework, before introducing the mechanisms and quantitative methods used to characterize thermal evolution during printing. The subsequent sections provide a critical synthesis of the reviewed literature, analyzing how thermal history mediates reported mechanical outcomes and identifying the key limitations and persistent challenges that remain in current FDM research. These insights motivate the proposed future research directions. The paper

concludes with a synthesis of the central role of cooling rate in shaping the thermal history and performance of ME-fabricated components.

2. Fundamentals of Cooling Rates in ME

The cooling rate in ME is a critical determinant of part quality, influencing dimensional accuracy, mechanical properties, and residual stress distribution [23]. This process involves the extrusion of thermoplastic filaments at elevated temperatures, followed by rapid solidification via conductive, convective, and radiative heat transfer mechanisms [22]. These heat transfer mechanisms govern the cooling rate, as it is a form of heat dissipation inside the layers of the printed parts, as well as the parts and the ambient environment [22]. Thus, the cooling rate controls how long the interface remains above the glass transition temperature (T_g), directly affecting interlayer bonding and porosity, which in turn reflects on the final strength of the printed part.

2.1. Heat Transfer Mechanisms

As the FDM process involves melting and extruding thermoplastic materials to build parts layer by layer, heat transfer plays a crucial role in the thermal characteristics of the process, which reflects on optimizing part quality, minimizing warping, and ensuring effective material adhesion. The heat transfer in ME can be explained through several mechanisms: conduction, convection, and radiation [24].

2.1.1. Conduction

Conduction is the primary mechanism of heat transfer in the ME process, occurring when heat is transferred through solid materials [11]. After extrusion, the molten filament is extruded onto the bedplate or the previous layer. Heat is conducted from the hot filament into the cooler substrate [25]. This conduction process helps melt the surface of the layer below slightly, which promotes adhesion between the newly deposited filament and the existing layer. This is critical for the structural integrity of the printed part [25]. Heat conduction can differ significantly between amorphous and crystalline polymers due to their distinct molecular structures and thermal properties [11]. Amorphous polymers typically have lower thermal conductivity compared to crystalline polymers. The random arrangement of their molecular chains means that heat can transfer less efficiently through the structure [26]. When heated, amorphous polymers gradually soften over a broad temperature range [26]. The absence of a sharp melting point means that heat conduction is a continuous process. In contrast, crystalline polymers generally exhibit higher thermal conductivity due to their ordered structure and the presence of crystalline regions, as shown in Figure 4 [27]. This ordered packing allows for a more efficient transfer of vibrational energy through the material [27]. This variety between them influences the cooling process where amorphous polymers adopt disordered cooling areas along the layers, which results in trapping residual thermal energy and may solidify without fully crystallizing [26]. In crystalline polymers, the heat conduction process during the cooling phase is also efficient, which leads the polymer to crystallize as it solidifies [26]. Thus, the material forms a crystal structure that has the ability to enhance dimensional stability and mechanical strength in the final printed part [28].

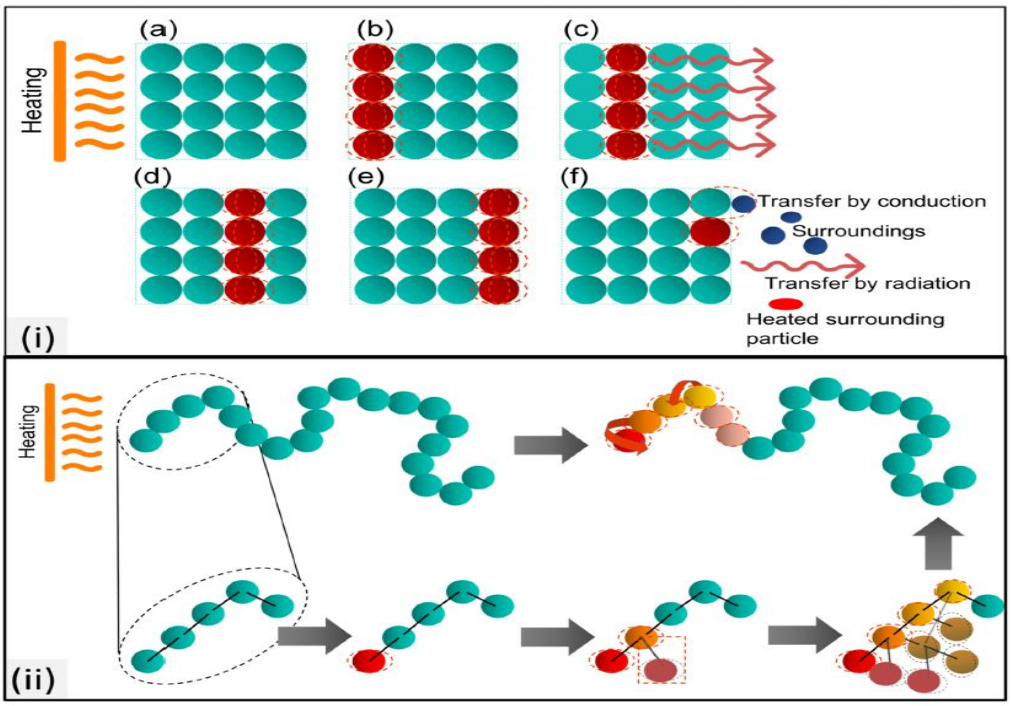


Figure 4. (**i**) How heat transfer occurs inside the crystalline polymer particles, where (a) represents the ideal order of the polymer lattices that start receiving heat. (b–e) illustrate efficient heat transfer within a perfectly arranged lattice structure, where thermal energy is sequentially conducted from one lattice element to the next. At stage (f), the outermost lattice at the polymer surface transfers heat by conduction when in contact with a solid surface, and by convection and radiation to the surrounding ambient environment.; (**ii**) how heat transfer occurs inside the amorphous polymer particles. The green circular regions represent amorphous polymer particles at room temperature. Upon heat input, these regions initially turn red, indicating the highest local temperature. As heat is transferred randomly through the amorphous polymer structure, a thermal gradient develops between neighbouring particles, which is visually represented by a gradual colour transition from red to yellow, where yellow denotes the lowest temperature prior to returning to room temperature [11].

The rate of conductive heat transfer (Q_{cond}) is modelled using Fourier's Law:

$$Q_{cond} = -k \cdot A \cdot \frac{\Delta T}{\Delta z} \quad (1)$$

where k is thermal conductivity ($W \cdot m^{-1} \cdot K^{-1}$), A is cross-sectional area, ΔT is temperature gradient, and Δz is layer thickness [29].

2.1.2. Convection

Convection heat transfer plays a critical role in determining cooling rates during the FDM process, influencing material solidification, interlayer bonding, and residual stress distribution [25]. In FDM, molten thermoplastic filaments are extruded and cooled via convective heat transfer to the environment. There are primarily two types of convection occurring in FDM: natural and forced convection [30]. Natural convection arises due to buoyancy-driven airflow caused by temperature differences between the heated polymer and cooler ambient air. As the deposited filament releases heat, the adjacent air layer warms, which causes a decrease in its density. Thus, it rises due to buoyancy. This upward motion is replaced by cooler ambient air moving toward the part surface, generating a sustained convective flow pattern that governs heat removal from the polymer [30]. The cooling rate under natural convection is typically slower, leading to prolonged solidification times. This can result in enhanced interlayer adhesion but may also induce warpage due

to uneven thermal contraction [23]. Conversely, forced convection involves active airflow, often generated by auxiliary cooling systems, which accelerates heat removal from the deposited layers. Enhanced cooling rates reduce the time available for molecular relaxation in the polymer, promoting rapid solidification [31]. While this minimizes warpage by reducing thermal gradients, excessive heat dissipation can compromise interlayer bonding and increase residual stress [23]. The rate of heat dissipation is governed by the convection coefficient h ($W \cdot m^{-2} \cdot K^{-1}$), which directly affects cooling times and thermal gradients. Higher h values accelerate cooling, reducing interlayer bonding time but potentially increasing residual stresses [30]. Therefore, manipulating cooling rates through convection control becomes vital for achieving the desired balance of mechanical properties and dimensional accuracy [5].

The rate of conductive heat transfer (Q_{conv}) can be modelled using Newton's Law of Cooling:

$$Q_{conv} = h \cdot A(T_s - T_\infty) \quad (2)$$

where h is the convective heat transfer coefficient ($W \cdot m^{-2} \cdot K^{-1}$), T_s is the surface temperature, and T_∞ is the ambient temperature [31].

2.1.3. Radiation

Radiation heat transfer plays a slight role in the thermal behaviour of the FDM process, which may be influencing both interlayer adhesion and cooling behaviour. The printer's nozzle emits heat radiation toward previously deposited layers during extrusion, which may elevate their surface temperatures and promote molecular diffusion across interfaces [32]. Also, radiative cooling from printed parts may contribute to thermal management. As layers solidify, they emit radiation proportional to their temperature and surface emissivity with losses modulated by environmental reflections and convective effects [33]. This radiative loss can influence the cooling rate of deposited layers, affecting crystallinity, residual stress distribution, and interlayer bonding. For instance, excessive radiative cooling may induce thermal gradients, promoting warping or delamination, particularly in semi-crystalline polymers [34]. Conversely, in enclosed printers with heated build chambers, radiative heat from the chamber walls can mitigate cooling rates, enhancing layer adhesion and dimensional accuracy [35]. However, the radiation effect is usually negligible in typical FDM processes due to low operating temperatures (<300 °C) [25].

The rate of radiative heat transfer (Q_{rad}) can be modelled using Stefan–Boltzmann law:

$$Q_{rad} = \varepsilon \cdot \sigma \cdot T^4 \quad (3)$$

where T represents absolute temperature, ε Surface emissivity (dimensionless, range (0–1)), and σ is the Stefan–Boltzmann constant (5.67×10^{-8} ($W \cdot m^{-2} \cdot K^{-4}$) [31].

2.2. Key Factors Influencing Cooling Rates

2.2.1. Material Thermal Properties

Material thermal properties are critical determinants of process stability, interlayer adhesion, and mechanical performance in ME process, as they govern heat transfer and cooling characteristics during extrusion, deposition, and solidification phases [11]. Thermoplastics commonly used in ME, such as acrylonitrile butadiene styrene (ABS), polylactic acid (PLA), and polyether ether ketone (PEEK), exhibit distinct thermal characteristics, including T_g, melting temperature (T_m), thermal conductivity (k), specific heat capacity (C_p), and coefficient of thermal expansion (α), each influencing print quality and structural integrity as described below.

- The glass transition temperature (T_g) is a temperature range where the polymer transitions from a rigid, glassy, and often brittle state to a more flexible, rubbery, or pliable state. Unlike the melting point (T_m), where a crystalline material changes from a solid to a viscous liquid, the glass transition is a transition in the material's mechanical properties, not a complete phase change [16]. The melting temperature, typically 20–50 °C above T_g for amorphous polymers like ABS, dictates the nozzle temperature required to achieve optimal viscosity for extrusion. In comparison, semi-crystalline polymers such as PEEK require precise control of T_m (≈343 °C) to prevent degradation [11]. Therefore, T_g is a fundamental material property that heavily influences thermoplastic behaviour during and after the FDM 3D printing process [11]. Because all surfaces that are in contact should be above the T_g to perform the adhesion process [16].
- Thermal conductivity (k), which usually ranges from 0.1–0.3 ($W \cdot m^{-1} \cdot K^{-1}$) for most polymers, regulates heat dissipation from the freshly extruded filament into the underlying substrate or the adjacent filament. Therefore, it is directly affecting the microstructure of the layers as well as influencing the cooling behaviour [26]. Because low k values contribute to thermal gradients, increasing residual stresses and warping due to uneven contraction during cooling, particularly in large prints [34].
- Specific heat capacity (C_p), representing the energy required to raise a material's temperature, influences the energy input necessary to achieve phase transitions [31]. It plays a critical role in the thermal management and process stability of FDM. Polymers with higher C_p, such as PLA ≈ 1.8 $J \cdot g^{-1} \cdot K^{-1}$, demand greater thermal energy for melting compared to ABS ≈ 1.3 $J \cdot g^{-1} \cdot K^{-1}$, which necessitates adjustments in nozzle heating power and extrusion rates to maintain consistent melt flow [11]. This property also governs the cooling dynamics of deposited layers, where materials with elevated C_p retain heat longer, resulting in slow solidification and promoting interlayer molecular diffusion, which enhances bond strength but risks deformation if cooling is insufficient [34].
- The coefficient of thermal expansion (α) expresses the material's tendency to change in length or volume for each degree of temperature change. In ME processes, this thermally driven deformation strongly influences dimensional stability, contributes to the build-up of residual stresses, and affects the final geometric accuracy of printed parts [11]. Polymers such as acrylonitrile butadiene styrene (ABS) and polylactic acid (PLA) exhibit α values ranging from 60–200 $\mu m \cdot m^{-1} \cdot K^{-1}$, whereas in semi-crystalline polymers like PEEK demonstrate anisotropic expansion due to crystallinity gradients [36]. High α values exacerbate residual stresses as uneven cooling rates between adjacent layers induce differential contraction, leading to warping, interfacial delamination, or interlayer cracking [37]. For instance, ABS (α ≈ 90–110 $\mu m \cdot m^{-1} \cdot K^{-1}$) is more prone to warping than PLA (α ≈ 60–70 $\mu m \cdot m^{-1} \cdot K^{-1}$), necessitating heated build plates to minimize thermal gradients and adhesion loss [37]. In semi-crystalline polymers, α is further complicated by crystallization kinetics. During cooling, regions of crystallinity contract more than amorphous domains, amplifying internal stresses and distorting part geometry. This necessitates precise control of bed temperature and cooling rates to regulate crystallization and mitigate dimensional inaccuracies [38].

Considering what is mentioned above about the material's thermal properties, recent advancements in in situ thermal monitoring have highlighted the need to optimize the parameters, such as bed temperature and cooling rates, to mitigate defects like delamination and warping, particularly in high-performance applications. Thus, understanding and tailoring process parameters to the thermal properties of FDM materials is indispensable for achieving mechanical robustness and geometric precision in the FDM process [11].

2.2.2. Effect of Process Parameters on Cooling Rate

Several parameters have a significant impact on the cooling rate behaviour during the process, which in turn affects the characteristics and production efficiency of the printed parts. Some of the most vital factors are nozzle temperature, bedplate temperature, printing speed, layer thickness and infill density.

- The extrusion temperature significantly impacts the cooling rate by determining the initial thermal state of the deposited material. Higher extrusion temperatures increase the material's fluidity, allowing for better layer adhesion but requiring longer cooling periods. Conversely, lower temperatures may lead to faster solidification but can compromise layer bonding [39]. The optimal temperature depends on the specific material properties, such as glass transition temperature and melt flow index, as shown in Figure 5. For instance, PLA typically requires lower extrusion temperatures (180–220 °C) compared to ABS (220–250 °C), affecting their respective cooling behaviours [40].

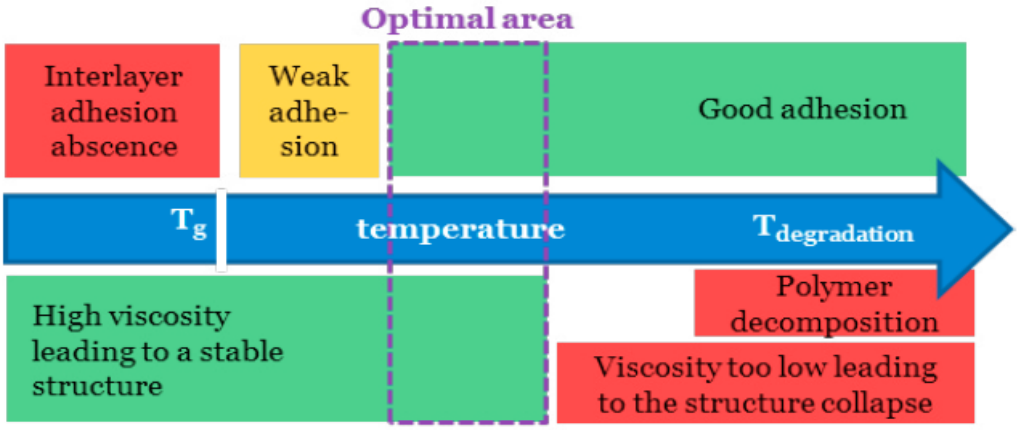


Figure 5. Optimal and non-optimal Nozzle temperature Effect on polymers [24].

- The bedplate temperature affects the cooling rate, particularly for the initial layers of the print. A heated build plate helps maintain the first layers at an elevated temperature, promoting better adhesion and reducing warping. However, it also slows the cooling rate of these layers [41]. The temperature gradient between the bedplate and the upper layers influences the overall cooling behaviour and internal stresses in part [42]. Different materials often require specific build plate temperatures for optimal results [43].
- Print speed influences the cooling rate by determining the time interval between successive layer depositions. While higher print speeds shorten the deposition cycle and reduce the time available for each layer to cool before the next one is applied, and the slower print speeds do the opposite, the actual inter-layer delay is also strongly dependent on the printed geometry. Larger cross-sectional areas, complex contours, or long tool-paths inherently extend the deposition time for a single layer, even at a constant print speed, thereby modifying the cooling window experienced by the material. Conversely, smaller or simpler geometries result in shorter toolpaths, resulting in shorter cooling intervals. These combined effects govern the accumulation or dissipation of heat within the part, influencing deformation phenomena such as warping and dimensional inaccuracy. Accordingly, the optimal print speed represents a balance between productivity and thermal control, and its effectiveness is closely linked to the geometric characteristics of the printed component [22,44].
- Layer height affects the cooling rate through its impact on thermal mass and heat transfer. Thinner layers have less thermal mass and thus cool more quickly than

thicker layers [45]. Additionally, thinner layers allow for more efficient heat transfer to the surrounding environment due to their increased surface area-to-volume ratio [33]. However, very thin layers may lead to longer print times and potential issues with material flow [46].

- Higher infill densities result in increased thermal mass within the printed part. This larger volume of material retains heat for longer periods, potentially slowing down the overall cooling rate [45]. Conversely, lower infill densities lead to reduced thermal mass, allowing for more rapid cooling. Also, the infill pattern and density affect heat distribution throughout the printed part [26]. Higher densities can lead to more uniform heat distribution, which may result in more consistent cooling rates across the object [35]. Lower densities, especially with certain infill patterns, can create air pockets that act as insulation, potentially leading to uneven cooling [22].

2.2.3. Geometry

The geometry of a part in FDM printing plays a crucial role in determining cooling rates by influencing heat transfer mechanisms, surface-to-volume ratios, layer characteristics, and thermal gradients [47]. In FDM, heat transfer occurs through conduction, convection, and radiation, and the geometry of the printed part significantly affects these mechanisms. Conduction within the printed part is primarily governed by its thickness and internal geometry, as described by Fourier's law (Equation (1)), since these factors determine the distance and pathways through which heat is transferred within the solid material. In contrast, characteristics such as surface area and the surface-to-volume ratio influence convective heat loss to the surrounding environment. Therefore, while geometry affects both mechanisms, its role in conduction pertains to internal heat flow, whereas its influence on convection is linked to the extent of the part's exposure to ambient air [48]. Parts with higher surface area to volume ratios generally cool faster due to increased exposure to the surrounding environment, whereas complex geometry creates non-uniform cooling rates across the object [49]. For example, complex geometries parts with sharp corners, overhangs, or thin walls experience heterogeneous cooling due to heat accumulation in localized regions, resulting in higher thermal gradients [50]. In practice, corner and thin-wall regions often warp due to steep thermal gradients, whereas large solid regions cool more slowly and more uniformly [42]. Because thicker layers retain heat longer, which in turn increases interlayer diffusion and reduces warping, but risks thermal degradation [51].

2.3. Mathematical Background for the Cooling Rates

Cooling rate is considered as a form of heat removal or heat dissipation from the newly deposited layer to the previous one and the ambient environment [22]. Therefore, it depends mainly on the modes of heat transfer, so the laws of heat transfer are the basis on which the cooling rate is based [45]. Both conduction and convection govern the cooling rates, whereas radiation is negligible in the usual FDM process [25]. These are described by Fourier's conduction law in Equation (4):

$$Q_{cond} = -k \cdot A \cdot \frac{\Delta T}{\Delta z} \tag{4}$$

where k is thermal conductivity ($W \cdot m^{-1} \cdot K^{-1}$), A is cross-sectional area, ΔT is temperature gradient, and Δz is layer thickness.

And Newton's law of cooling (convection) in Equation (5):

$$Q_{conv} = h \cdot A(T_s - T_\infty) \tag{5}$$

where h is the convective heat transfer coefficient ($W \cdot m^{-2} \cdot K^{-1}$), A is cross-sectional area, T_s is the surface temperature, and T_∞ is the ambient temperature.

Although both conduction and convection contribute to the overall cooling behaviour, they influence the process through different mechanisms. Conduction governs heat transfer within the printed part material itself, while convection is limited to the part's external surfaces. For this reason, determining the internal temperature field is the essential first step in evaluating the cooling rate, as it is fundamentally governed by the transient heat conduction equation:

$$\frac{\partial T}{\partial t} = \frac{k \cdot \nabla^2 T}{\rho \cdot c} \tag{6}$$

where k is thermal conductivity ($W \cdot m^{-1} \cdot K^{-1}$), $\boldsymbol{\rho}$ is density, $\boldsymbol{c}$ specific heat (for PLA, $\rho \approx 1240\ kg/m^3$, $c \approx 1800\ J \cdot kg^{-1} \cdot K^{-1}$; for ABS, $\rho \approx 1040\ kg/m^3$, $c \approx 1470\ J \cdot kg^{-1} \cdot K^{-1}$), T is temperature (K or °C), t is time (s), and $\nabla^2 T$ is the Laplacian of temperature, representing the spatial temperature variation [33].

Initially, this parabolic equation describes how the internal temperature evolves with time under the assumption of one-dimensional heat transfer (e.g., in the thickness of a filament) or even lumped (well-mixed temperature). In cases where the temperature within the body can be assumed uniform, the system may be treated using a lumped-capacitance model. To justify this simplification, the Biot number should be calculated, and it should be small (Bi < 0.1) [42]. It can be calculated by the following formula:

$$\mathrm{Bi} = \frac{h \cdot L_c}{k} \tag{7}$$

where L_c is the Characteristic length (m) and L_c = Volume (V)/Surface Area (A), k is thermal conductivity ($W \cdot m^{-1} \cdot K^{-1}$), and h is the convective heat transfer coefficient ($W \cdot m^{-2} \cdot K^{-1}$). The Biot number represents the ratio of internal conductive resistance to external convective resistance [31]. In this case, when Bi < 0.1, the internal conductive resistance is much smaller than the convective resistance, meaning that heat redistributes within the material far more rapidly than it is removed at the surface. As a result, the temperature inside the body remains nearly uniform, validating the lumped-capacitance assumption. Under this condition, the cooling behaviour follows Newton's law of cooling:

$$\frac{dT}{dt} = -\frac{h \cdot A}{\rho \cdot c \cdot V}(T_0 - T_\infty) \tag{8}$$

where h is the convective heat transfer coefficient ($W \cdot m^{-2} \cdot K^{-1}$), ρ is density, $\boldsymbol{c}$ is specific heat, V is volume, A is surface Area, T_0 is the layer surface temperature, and T_∞ is the ambient temperature. This formula represents temperature change over time, assuming uniform temperature distribution in a small body [42]. And when solving this, it gives:

$$T(t) = T_\infty + (T_0 - T_\infty) \cdot e^{\left(-\frac{h \cdot A}{\rho \cdot c \cdot V} \cdot t\right)} \tag{9}$$

This formula predicts the temperature of the body over time under Newtonian cooling.

However, when the Biot number exceeds 0.1, Convection removes heat faster than it can be redistributed internally, creating non-uniform temperature fields inside the filament. Thus, the lumped assumption fails, and the cooling process must be described by the distributed transient conduction model, a full conduction equation with spatial temperature dependence [31,42]. Analytical solutions exist for 1D or simple shapes (e.g., slabs, cylinders,

or semi-infinite domains) using Fourier series or error functions [52]. For example, a semi-infinite substrate solution can be described:

$$T(x,t) = T_\infty + (T_0 - T_\infty) \cdot \mathrm{erf}\left(\frac{x}{2 \cdot \sqrt{\text{Ƙ} \cdot t}}\right) \tag{10}$$

where erf is the error function (a special function), x is the depth from the surface (m), t is the time (s), and Ƙ is Thermal diffusivity (m^2/s) and $\text{Ƙ} = \frac{k}{\rho c}$. As for convection cooling with the ambient environment, a modified boundary condition should be defined, and it can be represented by:

$$\left(\frac{\partial T}{\partial x}\right)_{x=L} = \frac{h}{-k} \cdot (T_s(L,t) - T_\infty) \tag{11}$$

where k is thermal conductivity ($W \cdot m^{-1} \cdot K^{-1}$), h is the convective heat transfer coefficient ($W \cdot m^{-2} \cdot K^{-1}$). L represents the position along the spatial domain where the convective boundary condition is applied, $\left(\frac{\partial T}{\partial x}\right)_{x=L}$ represents the temperature gradient at the surface of the part ($x = L$ (K/m)), and $T_s(L,t)$ represents the surface temperature at position $x = L$ and time t (K or °C) [53]. In practice, because FDM involves 3D geometries and highly localized heating, numerical methods such as finite difference or finite element approaches are typically employed to capture the transient, spatially varying cooling behaviour [33].

The importance of cooling rate in the FDM printing process stems from its role, because it carves the thermal profile and history of the printing process and the interlayer bonds in FDM are controlled by the thermal history. Bonding between layers and threads occurs while the polymer interface is above T_g [22,53]. There are two key models that describe bond development in the FDM process. The first model is Viscous sintering (Frenkel's model) [54]. When two cylindrical filaments come into contact above T_g, they coalesce by viscous flow, driven by surface tension Γ [53]. Bellehumeur et al. (1998) [55] used a variant of Frenkel's model for cylinders. Defining the half-neck radius $y(t)$ between two filaments of initial radius a, one can introduce θ such that $y = a \sin\theta$. The growth is given by a nonlinear ODE:

$$\frac{d\theta}{dt} = \frac{\Gamma}{a_0 \cdot \mu} \cdot \frac{2^{-\frac{5}{3}} \cdot \cos\theta \cdot \sin\theta \cdot (2 - \cos\theta)^{\frac{1}{3}}}{(1 - \cos\theta) \cdot (1 + \cos\theta)^{\frac{1}{3}}} \tag{12}$$

where θ is the dynamic contact angle of the molten filament, t is time, μ is the polymer viscosity, Γ represents the surface tension of the molten polymer, and a_0 refers to the initial filament radius or characteristic radius after extrusion [55]. This equation arises from balancing the curvature-driven pressure ($\propto\Gamma$) with viscous flow ($\propto\mu$). As t increases, θ (and thus y) grows, meaning the neck, bonded area, widens. A higher surface tension and lower viscosity, featured in hotter filament, give faster neck growth [53]. Practically, this shows why printing at a higher nozzle temperature, resulting in lower μ, yields stronger bonds. However, once the material cools near T_g, μ rises and sintering effectively halts. Bellehumeur found that for ABS neck growth became negligible below ~200 °C, defining it as a critical sintering temperature [56].

The second model is Interdiffusion (welding time), which is used to predict the bond strength by describing the bond strength as a function of the temperature history [57]. Even without large viscous flow, polymer chains can diffuse across the interface. The strength gain can be modelled by a healing or degree of bonding $D_h(t)$ [53]. Yang et al. [57] used the following formulation:

$$D_h(t) = \frac{\sigma^*(t)}{\sigma_\infty} = \left[\int_0^t \frac{1}{t_w(T)} dt\right]^{\frac{1}{4}} \tag{13}$$

where $\sigma^*(t)$ is the transient bond strength, σ_∞ is the fully healed strength, and $t_w(T)$ is a welding time parameter. The factor 1/4 comes from reptation kinetics in polymer diffusion [57]. The welding time t_w depends on temperature via an Arrhenius law:

$$t_w(T) = C \cdot e^{\left(\frac{Q_d}{RT}\right)} \tag{14}$$

with material constants Q_d (activation energy), C is a pre-exponential constant, and R is the universal gas constant (≈8.314 J·mol^{-1}·K^{-1}). Bellehumeur reported an Arrhenius parameter set for ABS ($Q_d \approx$ 388,700 J/mol and $C \approx 1.08 \times 10^{47}$ s) corresponding to one of the boundary conditions examined in his model. Bellehumeur also examined alternative boundary assumptions, each producing its own parameter set [56]. Clarifying this distinction is essential, as the selection of boundary condition directly influences the fitted Arrhenius constants and, consequently, the predicted welding kinetics.

When T becomes less than T_g, diffusion effectively stops, and D_h saturates. This model aligns with the observation that a longer time at high T (e.g., heated build chamber or slow cooling) yields higher bond strength [53].

Together, these models show that bonding strength is a strong function of thermal history, which mainly relies on the cooling rate. Rapid cooling reduces the time above T_g, limiting neck growth and diffusion and leading to weaker interlayer bonds. In practice, ensuring the bead remains hot enough and long enough, by controlling ambient temperature or layer time, is key to strong parts.

A representative scenario was constructed for PLA and ABS filaments to show how cooling laws translate into bonding predictions. A deposited road of radius r = 0.20 mm was considered, with T_0 = 210 °C for PLA and T_0 = 240 °C for ABS. Ambient conditions were T_∞ = 25 °C (open air) and T_∞ = 50 °C (heated chamber), with h = 20 W·m^{-2}·K^{-1}. Table 1 shows the thermal properties for both PLA and ABS.

Table 1. Representative thermal properties for PLA and ABS.

Material	Q (kg·m^{-3})	C_p (J·kg^{-1}·K^{-1})	k (W·m^{-1}·K^{-1})	T_g (°C)	Source
PLA	1240	1800	0.13	60	[58,59]
ABS	1100	900	0.10	105	[56,60]

With Bi ≈ 0.015 for PLA and Bi ≈ 0.020 for ABS, the values remain well below 0.1, validating the lumped-capacitance assumption. Therefore, from Equation (9), the cooling law:

$$T_t - T_\infty = (T_0 - T_\infty)e^{\left(\frac{-t}{\tau}\right)}, \tau = \frac{\rho \cdot c \cdot V}{h \cdot A} \tag{15}$$

where h is the convective heat transfer coefficient (W·m^{-2}·K^{-1}), ρ is density, c is specific heat, V is volume, A is surface Area, T_0 is the layer surface temperature, and T_∞ is the ambient temperature. This was used to compute the time until the glass transition (t_{T_g}):

$$t_{T_g} = \tau \cdot \ln\left(\frac{T_0 - T_\infty}{T_g - T_\infty}\right) \tag{16}$$

PLA remained above T_g for 18.6–30.9 s, while ABS remained above T_g for 4.9–6.1 s, as shown in Figure 6. Bond formation was then modelled. For viscous sintering, the Frenkel relation:

$$\left(\frac{x}{a}\right)^2 = \frac{\Gamma}{3a}\int_0^t \frac{dt'}{\mu(T(t'))} \tag{17}$$

was applied with Γ = 0.03 N·m^{-1}. Viscosity followed an Arrhenius law, and activation energies of 70 kJ·mol^{-1} for PLA and 110 kJ·mol^{-1} for ABS were selected from rheological

and welding studies, consistent with reported ranges for amorphous polymers [56,61]. Integration (Python, version 3.10) yielded neck ratios of 0.42–0.46 for PLA and 0.17–0.19 for ABS, confirming larger bonded areas for PLA, as Figure 7 shows. For chain interdiffusion, reptation-based constants for ABS, (Q_d = 388.7 kJ·mol^{-1}, $C = 1.08 \times 10^{47}$ s) from [56], predicted negligible healing because dwell time, the duration for which the interface remains above the glass-transition temperature after deposition, was extremely short. For PLA, consistent reptation constants are lacking in the literature. To enable comparison, a normalized Arrhenius index W was defined, derived from the temperature dependence of reptation models but without a polymer-specific prefactor. This index is not an absolute healing fraction but a relative measure, allowing assessment of how thermal history influences chain interdiffusion. This index showed ~18% higher values at 50 °C versus at 25 °C, which indicates improved interdiffusion in a heated chamber, as shown in Figure 8. All the cooling and bond-formation metrics are shown in Table 2.

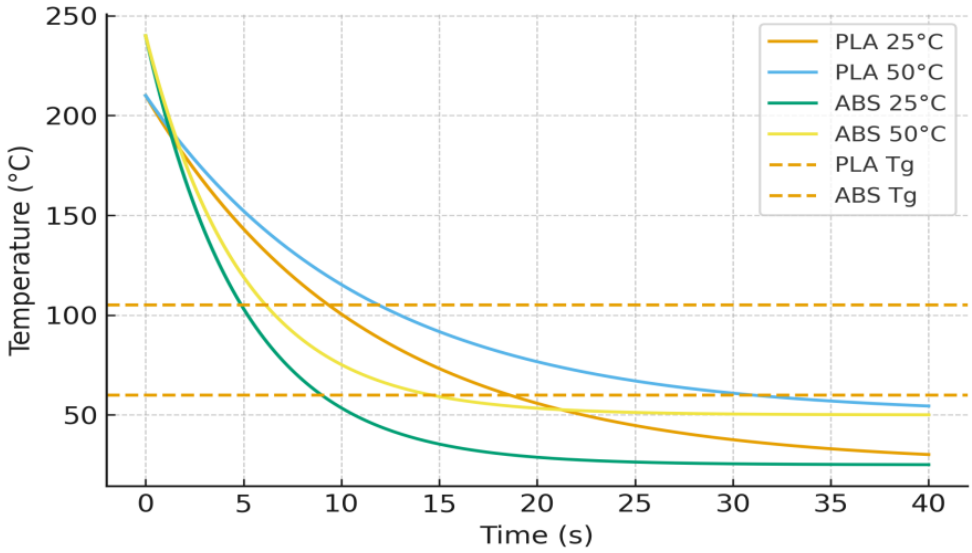


Figure 6. Cooling histories of PLA and ABS filaments predicted by the lumped-capacitance model under two ambient conditions.

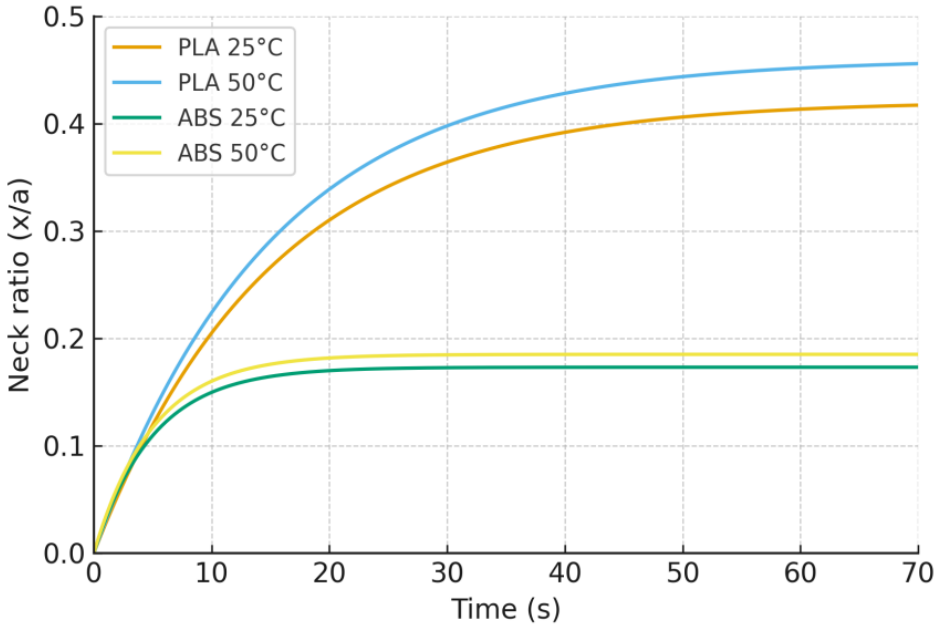


Figure 7. Evolution of the interfacial neck ratio (x/a) between adjacent roads.

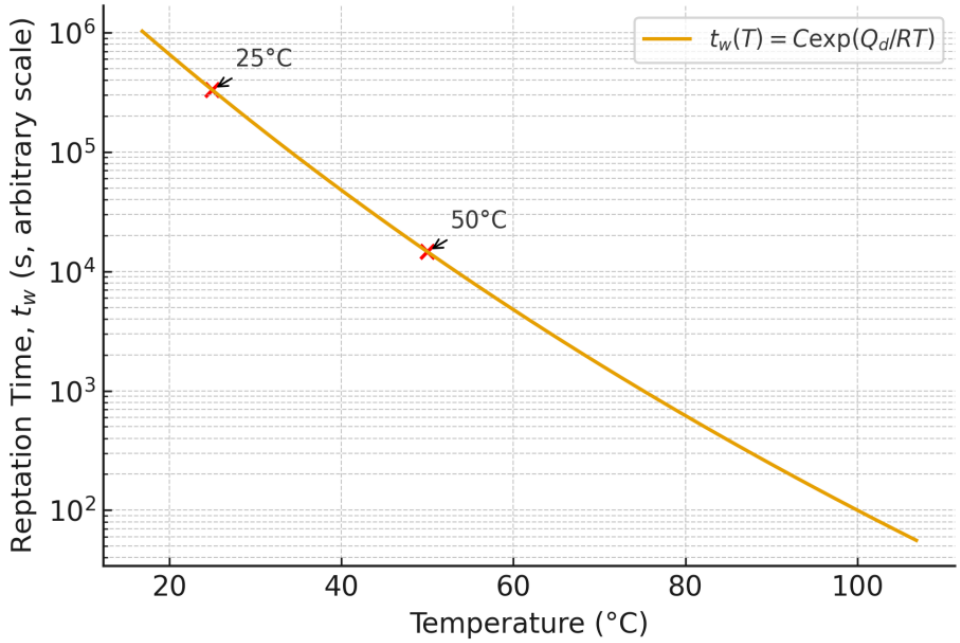


Figure 8. Schematic of the Arrhenius dependence of reptation time, $t_w(T) = C{\cdot}e^{\left(\frac{Q_d}{RT}\right)}$. A modest increase in chamber temperature (25 °C → 50 °C) exponentially reduces t_w, enabling greater chain mobility and interdiffusion.

Table 2. Cooling and bond-formation metrics (h = 20 W·m^{-2}·K^{-1}).

Material	Ambient (°C)	t_{T_g} (s)	Neck Ratio x/a	Healing Metric
PLA	25	18.6	0.421	$W = 2.53 \times 10^{-10}$
PLA	50	30.9	0.460	$W = 2.99 \times 10^{-10}$ (+18%)
ABS	25	4.9	0.173	$D_h \approx 0$
ABS	50	6.1	0.185	$D_h \approx 0$

3. Role of Cooling Rate in FDM

Cooling rate during and after deposition governs how long the interlayer interface remains above the glass transition or melting temperature, which directly controls polymer chain diffusion, entanglement, the development of weld strength, and porosity [56,57]. For semi-crystalline systems such as polyamides, polylactic acid (PLA), and polyetheretherketone (PEEK), the local cooling history also determines crystallization kinetics, spherulite growth, and interfacial crystallinity, thereby influencing stiffness, toughness, and dimensional stability [11,28,37].

3.1. Cooling Rate Effect on Crystallinity and Microstructural Morphology

The degree of crystallinity in semi-crystalline ME polymers decreases as the cooling rate increases, because rapid quenching limits the time available for chains to organize into ordered structures [11,28]. For polyamides, work combining ME-like cooling histories with crystallization analysis indicates that increasing cooling rate from a few °C/s to hundreds of °C/s can reduce crystallinity by roughly one-third, with clear consequences for stiffness and heat resistance [11,28]. In PEEK, raising the chamber temperature from ambient (≈25 °C) to about 200 °C can increase crystalline content from approximately 17% to approximately 31%, as slower effective cooling reduces internal stresses and allows more complete crystal growth [11,31].

Similar trends are reported for PLA: slow-cooled specimens can show crystallinity values around the high-30% range, whereas actively fan-cooled parts may exhibit crystallinity

lower by several percentage points, associated with reduced impact strength and thermal resistance [11,15,45,50]. Cooling rate also shapes crystal morphology, as slow cooling or isothermal dwells near the melting temperature yield larger spherulites and transcrystalline regions, while rapid cooling or low-temperature dwells produce smaller, more fragmented spherulites and sharper crystallinity gradients [11,28,50]. Consequently, tuning cooling rate and thermal dwell conditions defines a process window for optimizing both crystallinity level and microstructural uniformity [11,24,25,50].

3.2. Cooling Rate Effect on Defect Formation

3.2.1. Warping Mechanisms

Warping in ME arises from non-uniform cooling and solidification, which cause differential shrinkage between rapidly cooling regions—such as corners, thin walls, and upper surfaces—and thermally retained areas like the interior and near-bed layers [20,41,47]. This uneven contraction induces bending moments that lift edges and distort planar geometry [20,41,47]. Numerical and experimental studies show that warpage magnitude increases with the steepness of through-thickness thermal gradients and the rate at which material drops below T_g for amorphous polymers or T_m and crystallization onset for semi-crystalline materials [18,20,25,42]. Process adjustments that are attributed to reduced thermal gradients effectively suppress warpage [18,20,34,41]. Higher print speeds minimize layer-to-layer cooling intervals, while elevated chamber temperatures limit convective heat loss and delay solidification [12,16,18,35]. For high-temperature polymers such as PEEK, the use of heated chambers, radiant heaters, or heat-retention systems can maintain the part at elevated temperature during deposition, reducing thermal gradients by more than half [11,18,32,35]. Such measures have been shown to decrease warpage by several times, in some cases limiting dimensional deviation to just a small percentage [20,41,47,51].

These improvements stem from slower and more uniform cooling, longer residence of the material above its mobility threshold, and more homogeneous viscoelastic stress relaxation, all of which reduce the driving force for differential shrinkage and improve dimensional stability.

3.2.2. Delamination and Interlayer Bonding

Cooling rate is a primary determinant of whether adjacent filaments in fused deposition modelling develop strong interlayer bonds or remain prone to delamination [23,24,56]. Bond formation requires the underlying filament to stay above the chain-mobility threshold (T_g for amorphous polymers and crystallization onset for semi-crystalline polymers) long enough to allow reptation, interdiffusion, and entanglement across the interface [23,54,56,57]. Slower cooling extends this diffusion-active period, generating a deeper, more coherent weld with higher entanglement density and improved toughness [23,54,56,57]. Even modest reductions in cooling rate or slight increases in interfacial temperature can substantially lengthen this weld time, leading to marked improvements in interlayer strength and resistance to layer separation [23,24,56].

Conversely, rapid cooling truncates the interval during which chains can interpenetrate the interface [23,56,57]. Once the temperature falls below T_g or crystallization onset, diffusion halts prematurely, producing a shallow, weakly entangled weld that behaves as a brittle plane [23,54,56,57]. Because chain mobility is highly temperature-dependent, small increases in cooling rate can disproportionately reduce weld time [23,54,57].

3.2.3. Residual Stress Accumulation

Residual stresses accumulate through repeated heating and cooling cycles as new material is deposited over constrained partially solidified layers, leading to non-uniform contraction through the part's thickness [18,20,30]. High cooling rates and steep ther-

mal gradients intensify these stresses by limiting the time available for viscoelastic relaxation and causing strain to be locked in as the material passes below T_g or crystallization onset [18,20,25,30]. This accumulation contributes directly to warpage, interlayer cracking, and loss of dimensional accuracy [18,20,24,30].

More uniform thermal profiles slow the cooling process and allow partial relaxation before stresses are frozen into the structure [18,24,25,32]. For high-temperature polymers such as PEEK and PEI, near-isothermal build environments can substantially reduce residual-stress magnitude [11,18,32,33]. Also, post-process thermal treatments, including annealing above T_g for amorphous polymers or controlled recrystallisation for semi-crystalline materials, further relieve internal stresses by enabling chain mobility and structural relaxation, significantly decreasing warpage and crack formation [11,28,31].

Overall, residual stress in material extrusion is a controllable thermal phenomenon rather than an inherent limitation of the process. Through carefully managed cooling processes and targeted post-processing, stress accumulation can be substantially reduced, leading to improved dimensional stability, fewer defects, and more reliable ME-fabricated components.

4. Previous Work and Research on FDM Process Parameter Optimization and Its Interactions with Cooling Rate

Establishing precise process conditions is paramount for each application to meet client specifications and ensure satisfaction. In FDM, numerous interacting parameters can individually or collectively affect the final part's quality. Therefore, it is crucial to identify the optimal combination of these process parameters because it has a noteworthy improvement in manufacturing efficiency and the quality of the produced parts. Therefore, extensive research has been dedicated to understanding how FDM process parameters impact mechanical performance and other key part attributes.

Previous optimization studies in FDM have historically focused on process parameters such as nozzle temperature, layer height, infill density, print speed and build orientation, yet many of these parameters exert their influence primarily through their effects on cooling rate, thermal gradients and the resulting thermodynamic behaviour of the polymer melt. The rapid or delayed cooling of deposited filaments governs mesostructural development, including interlayer diffusion, crystallization kinetics, void formation, warping and delamination, and ultimately determines the mechanical and thermal performance of the final part. However, earlier studies often reported mechanical or microstructural outcomes without explicitly connecting them to the underlying cooling profile.

To address this, the following review reorganizes prior work for PLA, ABS and other polymers while explicitly reframing each study in terms of how the chosen parameters modulate cooling rate, crystallinity and defect formation. This approach more directly reveals the thermal mechanisms guiding part quality, thereby aligning with the thermodynamic focus of this review. Each of these sections will arrange the previous work chronologically from 2019 to date. PLA and ABS are given dedicated sections due to their status as the most widely adopted and extensively researched thermoplastic filaments in FDM [6].

4.1. Polylactic Acid (PLA)

In 2019, Luzanin et al. [62] carried out a systematic investigation on PLA using a Box–Behnken design of experiments (DoE) with four input parameters: layer thickness, extrusion speed, nozzle temperature, and bed temperature. Mechanical characterisation was performed through tensile testing, while differential scanning calorimetry (DSC) was used to quantify crystallinity. Their results demonstrated that layer thickness and its interaction with extrusion speed were the most influential factors shaping tensile properties. While

their analysis showed that crystallinity could be increased by parameter adjustments, this did not directly correlate with mechanical strength. The interaction they observed between layer thickness and extrusion speed indicates strong modulation of the cooling profile, as thicker layers cool more slowly but retain internal thermal gradients that can impede uniform weld development. Their finding that crystallinity did not directly correlate with tensile performance reinforces that the decisive factor is the thermal state of the interlayer interface where insufficient time above the glass transition temperature limits polymer-chain mobility, preventing adequate diffusion across bead boundaries. This suggests that the cooling rate, not bulk crystallinity, is the primary mechanism governing mesostructural consolidation in their parameter window.

In the same year, Aloyaydi et al. [63] explored the role of infill density in determining the flexural behaviour and microstructure of PLA. Their tests showed that increasing infill density improved load-bearing ability, as shown in Figure 9, while very high density promoted a shift from brittle to ductile fracture modes. Microscopy confirmed that greater density reduced porosity and strengthened interlayer adhesion, highlighting how internal architecture affects performance. However, the study did not consider wider parameter variations such as speed or temperature, which could have influenced the results. Still, their findings underline that the improvement in flexural behaviour at higher infill densities aligns with a slower internal cooling regime, as densely packed rasters retain heat for longer durations and promote a more stable interlayer weld. This extended thermal contact reduces premature solidification, allowing more complete diffusion of molecular chains. The shift from brittle to ductile fracture modes mirrors this enhanced thermal history, indicating more uniform bonding and lower void concentration.

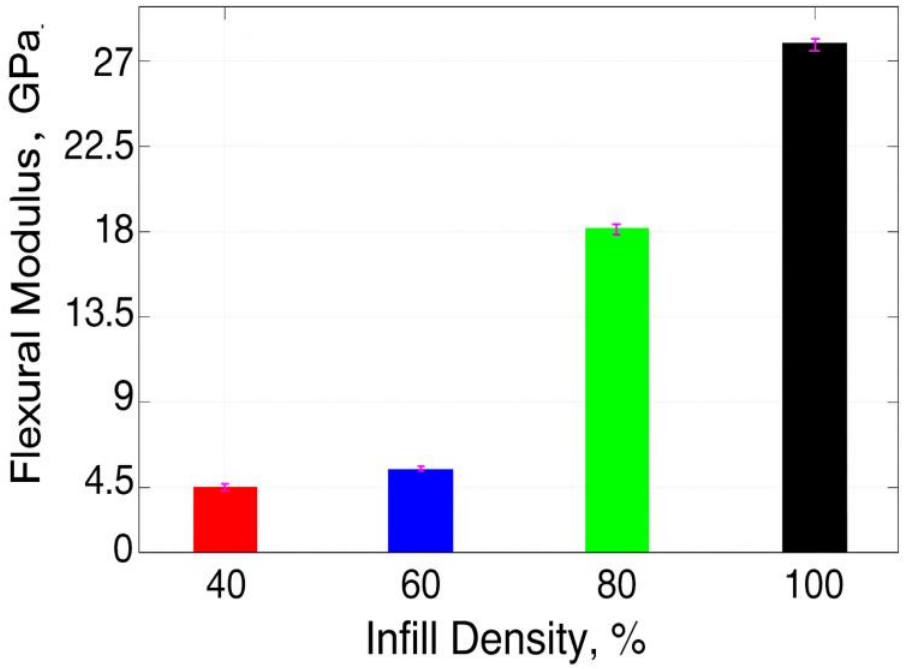


Figure 9. Influence of infill density on flexural modulus, The pink bars typically represent variability or uncertainty in the measured flexural modulus [63].

Then, Tang et al. [64] examined PLA lattice structures by applying a full factorial DoE that explored the effects of printing temperature, print speed, layer thickness, and shell thickness. Tensile and compressive testing were supported by scanning electron microscopy (SEM) to characterise fracture features. They observed that higher nozzle temperatures and lower print speeds reduced porosity and improved interlayer fusion, although excessive heating introduced brittle behaviour. The scope of the study was limited by its narrow set

of process parameters and the absence of crystallinity analysis. Nevertheless, their findings demonstrate that the reduction in porosity at higher nozzle temperatures and lower speeds illustrates how increased thermal input prolongs the molten state of deposited strands, thereby delaying cooling and enabling deeper interdiffusion. Their observation of brittle failure at excessive temperatures is also thermally driven, as overheating induces abrupt crystallization or residual stresses once cooling finally occurs. These results highlight that both insufficient and excessive cooling can degrade interlayer integrity in different ways.

Also in 2020, Cardoso et al. [65] investigated PLA/PBAT blends through a Taguchi orthogonal array DoE, focusing on flexural behaviour with supporting microstructural observations. They reported that thinner layer heights combined with slower deposition speeds produced denser and mechanically stronger parts, whereas thicker layers and faster deposition promoted porosity and weak adhesion. Microscopy confirmed that when cooling was more gradual, the material fused more effectively across layer boundaries. The study was limited to flexural behaviour without exploring tensile or impact properties, but it strongly illustrates that the microstructural improvements reported at thin layers and slow deposition speeds correspond directly to a smoother cooling trajectory, which maintains the interface above the glass transition longer and allows stronger weld formation. Conversely, thicker layers accumulate thermal gradients that promote uneven shrinkage during cooling, increasing the likelihood of pore entrapment. Their findings reinforce that the thermal history of the layer interface is more influential than geometric parameters alone.

Later in 2021, Von Windheim et al. [66] combined process parameter optimisation with annealing treatments to address anisotropy in PLA prints. Tensile testing and DSC analysis showed that annealing below the cold crystallisation temperature (T_{cc}) improved weld interfaces without substantially changing crystallinity, whereas annealing above this point increased crystallinity but did not improve strength. The contrast between annealing below and above T_{cc} demonstrates the delicate balance between cooling rate and polymer mobility. Sub-T_{cc} annealing enhances weld strength because it locally reheats the interface without triggering excessive crystallization that would lock chains prematurely. In contrast, annealing above T_{cc} increases crystallinity but lowers interlayer toughness due to restricted chain motion. Thus, their results emphasize that cooling-mediated weld healing is more important than crystallinity enhancement.

Also in 2021, Hikmat et al. [67] applied the Taguchi method across seven factors: build orientation, raster angle, nozzle diameter, extrusion temperature, infill density, number of shells, and print speed. In Figure 10, Tensile results showed that build orientation was most significant, followed by nozzle diameter and infill density. Although microstructural evaluation was not directly performed, the findings suggest that the influence of build orientation on tensile performance reflects how different raster paths dissipate heat in distinct ways. Vertical and angled orientations tend to cool faster along unsupported features, reducing interlayer diffusion and forming weaker welds compared to orientations where adjacent strands exchange heat. Even without microstructural analysis, their ranking of parameter significance strongly aligns with known thermal-path dependencies in PLA.

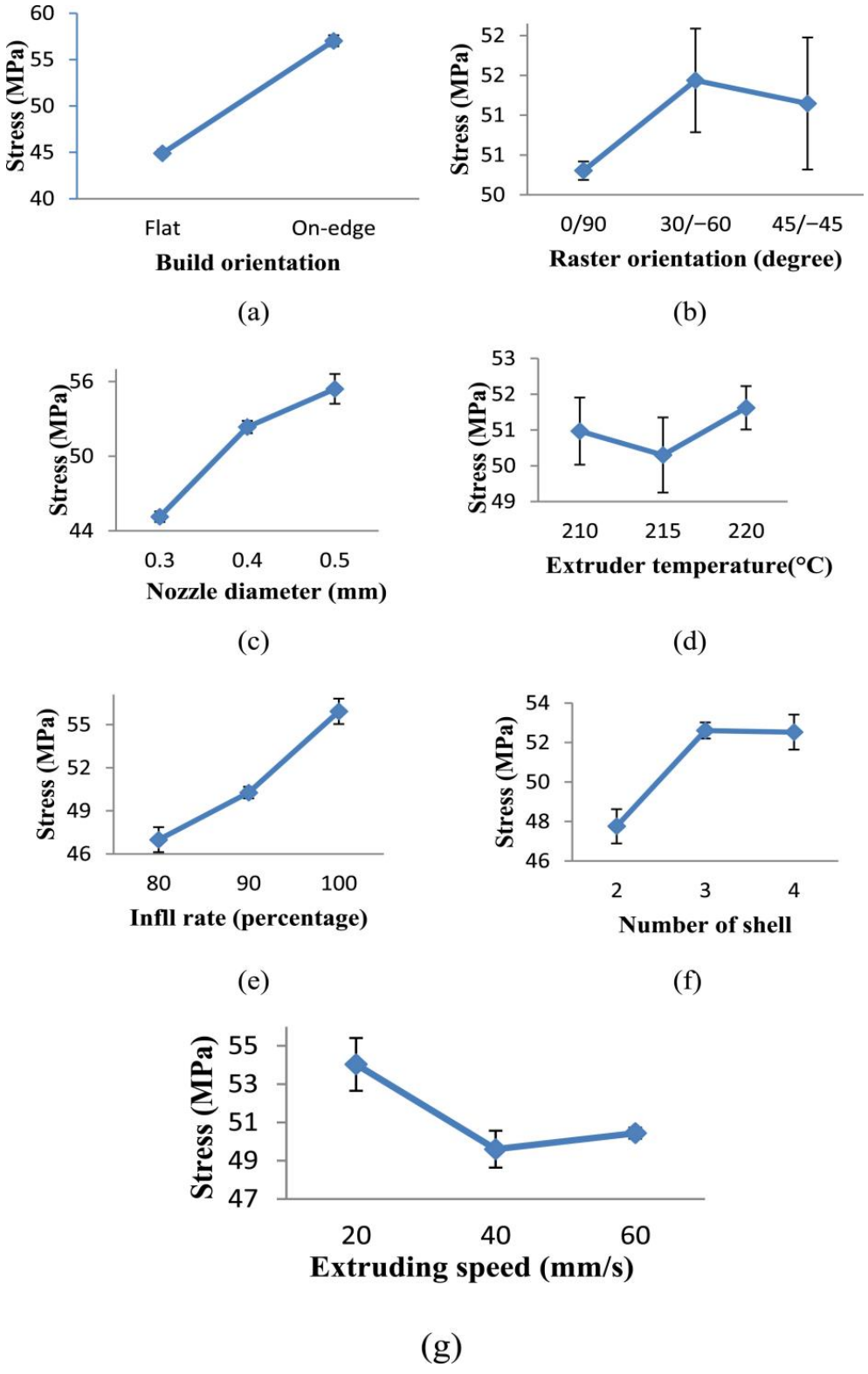


Figure 10. Stress–strain responses corresponding to each parameter. (**a**) shows the effect of build orientation, (**b**) shows the effect of raster orientation, (**c**) shows the effect of nozzle diameter, (**d**) shows the effect of extruder temperature, (**e**) shows the effect of infill rate, (**f**) shows the effect of number of shells, and (**g**) shows the effect of extruding speed [67].

A year later, Kamer et al. [68] investigated the effect of print speed on porosity and strength by performing tensile testing and porosity analysis. They found that faster deposition resulted in more air gaps and weaker bonding. The study was somewhat narrow in

scope, but it clearly demonstrates that the increased porosity and reduced strength at higher printing speeds directly correspond to shorter thermal exposure times between successive rasters, causing premature cooling before adequate bonding occurs. Slower speeds extend the "thermal overlap" window, allowing the underlying layer to reheat sufficiently for improved diffusion. These behaviours are characteristic indicators of cooling-dominated interlayer failure mechanisms.

As for Auffray et al. [69], they explored multiple parameters using analysis of variance (ANOVA), including infill density, infill pattern, layer thickness, print speed, raster orientation, overlap, and extrusion temperature. Their results indicated that infill density and pattern were most influential for elastic properties. The stronger elastic performance associated with dense infill and certain patterns stems from enhanced thermal retention within the internal structure, producing smoother cooling gradients and reducing void growth. Sparse infills cool rapidly due to larger air gaps, leading to incomplete fusion and micro-porosity. Their ANOVA results indirectly map how the internal cooling environment interacts with structural patterns to shape mechanical behaviour.

Also in 2023, Kumar et al. [70] employed response surface methodology (RSM) to optimise tensile, flexural, and impact strength. They concluded that thinner layers and moderate speeds improved bonding and reduced crack propagation, as shown in Figure 11. The improvements in tensile, flexural and impact strength under thin-layer, moderate-speed conditions reflect slower and more uniform cooling at the interlayer region. These conditions minimize shrinkage-induced stress accumulation and facilitate extended chain mobility. As a result, the fracture behaviour becomes consistent with thermally stabilized weld regions where diffusion has reached a more advanced stage.

Moreover, Ahmed et al. [71] incorporated annealing into their optimisation strategy, combining tensile testing and SEM analysis. They showed that heat treatment enhanced strength by promoting interlayer diffusion. However, the study did not measure porosity or crystallinity changes after annealing, leaving a gap in understanding the underlying structural changes. Nevertheless, the findings strongly reinforce that the strengthening effect of annealing can be understood as a controlled reactivation of the weld interface, temporarily reversing the rapid cooling experienced during deposition and allowing additional molecular bridging to occur. Even without porosity or crystallinity measurements, the SEM images indirectly confirm that reheating moderates earlier thermal gradients, reducing weakly bonded regions. This demonstrates the corrective potential of post-deposition thermal conditioning.

However, in 2023, Delbart et al. [72] analysed PLA composites using a DoE approach that considered nozzle diameter, raster angle, and layer thickness. Mechanical testing revealed that ductility was influenced more by crystallinity than by porosity. The limitation of their work was the narrow mechanical focus without exploring fatigue behaviour. Even though their identification of crystallinity as a driver of ductility underscores how deposition geometry affects the cooling trajectory and subsequent crystal development. Larger raster angles or nozzle diameters introduce distinct cooling rates across the cross-section, producing spatially heterogeneous crystallinity. Their findings show that thermal gradients, not voids alone, can determine macroscopic deformation behaviour.

In the same year, Popović et al. [73] investigated nozzle temperature and speed using tensile testing and surface roughness analysis. They demonstrated that moderate heat combined with low speeds improved strength and dimensional accuracy. Although the scope was limited to dimensional accuracy and tensile strength, their work provides additional evidence that the balance between dimensional accuracy and mechanical strength they observed arises from competing cooling requirements where rapid cooling stabilizes geometry but restricts interlayer healing, while slower cooling enhances bonding at the

expense of precision. Therefore, their optimal window reflects a thermal compromise that maintains interface temperature long enough for diffusion while limiting thermal deformation. This trade-off typifies PLA's sensitivity to cooling-driven shrinkage.

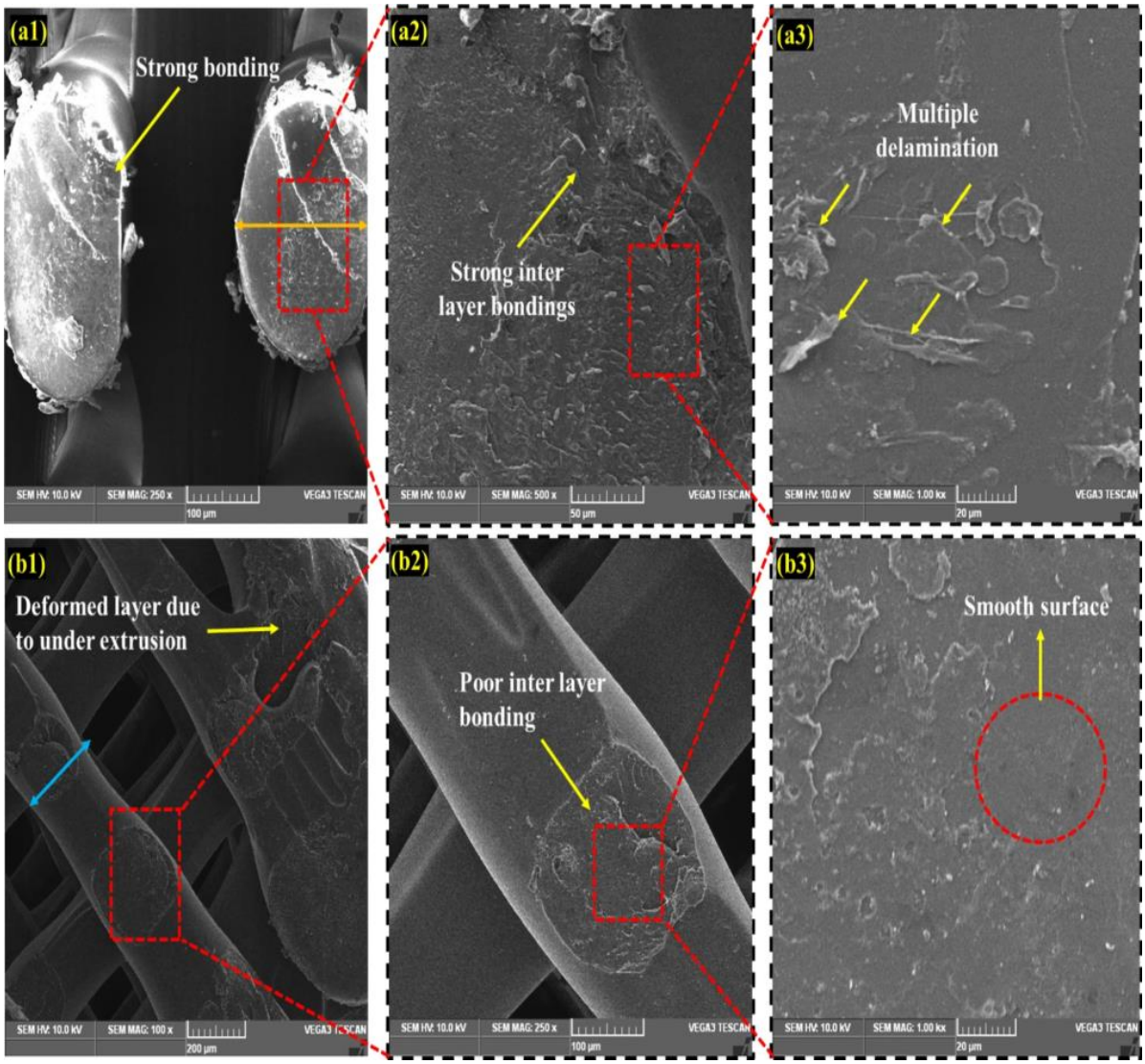


Figure 11. Comparison of fracture mechanism of tensile specimens (**a1**–**a3**), optimum parameters and (**b1**–**b3**) un-optimum parameters [70].

While Wang et al. [74] examined large-format extrusion, evaluating nozzle diameter, bead width, and infill orientation through flexural testing and void morphology analysis. They found that bead width dictated inter-bead void formation, which influenced strength. The strong influence of bead width on void formation directly results from thermal mass effects, where thicker beads cool more slowly and promote stronger fusion, while narrow beads lose heat rapidly and trap voids. Their flexural results correlate with the magnitude of these thermal gradients. This highlights that extrusion geometry acts primarily as a cooling-rate modifier in large-format printing.

Recently, in 2024, Cadete et al. [75] studied crystallinity in PLA using a multi-factor DoE with deposition speed, bed temperature, nozzle temperature, fan speed, and flow rate. DSC and tensile testing showed that slow speeds and high bed temperatures yielded higher crystallinity. Their crystallinity trends confirm that slow deposition speeds and elevated bed temperatures shape the cooling curve in ways that favour crystal growth. High fan speeds or rapid deposition accelerate cooling and suppress ordering. While the study did

not link these structural changes to strength, the cooling rate dependence of crystallinity is clearly demonstrated in their DSC data.

At the same time, Gajjar et al. [76] optimised tensile strength through a Taguchi method involving nozzle temperature, layer thickness, and raster angle. Using tensile testing and SEM, they concluded that thinner layers and higher extrusion temperatures enhanced fusion. The study could have been strengthened by examining fracture behaviour, but it still shows that enhanced fusion at high extrusion temperatures and thin layers reflects longer dwell times above T_g, allowing greater interpenetration of polymer chains before solidification. Their SEM observations of smoother interfaces are consistent with reduced cooling gradients and more complete weld development.

Also in 2024, Faizaan et al. [77] combined the Taguchi method with micro-computed tomography (μ-CT) to link printing conditions with void architecture. They demonstrated that large nozzles combined with fine layers minimized porosity and improved reproducibility. The study's scope was limited to PLA only, without exploring blends or composites, but it robustly established the link to cooling rate, since the reduced porosity observed under large-nozzle and fine-layer conditions indicates a controlled thermal decay where heat is dissipated gradually rather than abruptly. That confirms that such thermal stabilization suppresses void nucleation across the cross-section.

In another 2025 study, Akhoundi and Jahanshahi [78] analysed single-layer PLA structures using tensile testing and SEM. They reported that inter-raster bonding improved at higher nozzle temperatures and wider extrusion widths. They attributed the improvement to reduced temperature drop at the deposition interface, which allowed better molecular diffusion across adjoining rasters. While the study was limited to single-layer specimens, it reinforced the point that reducing thermal gradients between rasters enhances molecular diffusion and strengthens bonding.

Moreover, Kechagias et al. [79] investigated vertical PLA printing through an ANOVA-based DoE. They varied nozzle temperature, extrusion flow rate, and speed, while measuring flexural behaviour and surface roughness. Their findings indicate that higher thermal input improved flexural performance and surface quality. Microscopy revealed that stronger interlayer fusion occurred under moderated cooling. The limitation is that only vertical orientation was explored, but the work provides strong evidence that thermal input and subsequent cooling behaviour dictate the integrity of interlayer bonding.

Lastly, Layeb et al. [80] focused on biomedical PLA liners using tensile testing and SEM. They demonstrated that thin layers and low raster angles provided strong bonding and minimal porosity. Microscopy showed well-fused interfaces under these conditions. Although the scope was limited to implant geometries, the findings emphasize that thin layers and low raster angles promote more uniform cooling across the thickness of their biomedical liner structures, enabling more cohesive weld formation and reduced porosity. The consistent interlayer fusion seen in SEM images aligns with conditions expected to minimize thermal discontinuities during deposition.

To synthesize the effects of process parameters on cooling dynamics, microstructural evolution, and mechanical performance in PLA, Table 3 provides a comparative overview of previously reported experimental studies, correlating processing conditions with cooling-induced microstructural features, interlayer bonding quality, and the resulting mechanical responses, together with the optimal parameter combinations identified in the literature.

Table 3. Comparative summary of PLA studies.

Author	Parameters Studied	Cooling/Microstructure Effects	Mechanical Outcomes	Optimal Settings
Luzanin et al. [62]	Layer thickness, extrusion speed, extrusion temp, bed temp	Thin layers & slow speeds → reduced porosity, stronger bonding	Max tensile strength, crystallinity ≈ 19.6%	0.2 mm LT, 30 mm/s, 230 °C nozzle, 50 °C bed
Aloyaydi et al. [63]	Infill density	Higher infill = lower porosity, shift from brittle to ductile	Optimal flexural strength & toughness at 80% infill	80% infill
Tang et al. [64]	Printing temp, speed, LT, shell thickness	Higher temp → less porosity but brittle fracture; slower speeds improved fusion	Tensile ≈ 51.5 MPa; Elastic modulus ≈ 5102 MPa	230 °C, 60 mm/min
Cardoso et al. [65]	LT, deposition speed, build direction	Thin layers + low speed → denser parts, better bonding	Flexural ≈ 52.5 MPa vs. ≈23.2 MPa at worst settings	0.10 mm LT, 40 mm/s, 0° build
Von Windheim et al. [66]	LT, speed, orientation, annealing	Sub-T_{cc} anneal healed welds; crystallinity increase alone ineffective	UTS: 64 MPa (XY), 37 MPa (YZ)	0.1 mm LT, 20 mm/s, 65 °C anneal
Hikmat et al. [67]	Orientation, raster, nozzle dia., temp, infill, shells, speed	Build orientation largest effect on cooling paths and bonding	Build orientation: 44.7% influence; nozzle dia. 0.5 mm & 100% infill optimal	On-edge orientation, 0.5 mm nozzle, 100% infill
Kamer et al. [68]	Print speed	High speeds ↑ porosity, ↓ strength; slower speeds ↓ voids	Tensile strength decreased sharply at >80 mm/s	≤30 mm/s
Auffray et al. [69]	Infill pattern, LT, infill density, speed, raster, overlap, temp	Dense infill retained heat, reduced porosity	Infill density & pattern most significant	100% infill, optimized pattern
Kumar et al. [70]	LT, speed, nozzle temp	Thin layers & moderate speeds improved crack resistance	Tensile ≈ 45.5 MPa; Flexural ≈ 78.5 MPa	0.10 mm LT, 60 mm/s, 200 °C
Ahmed et al. [71]	Infill density, pattern, LT, nozzle temp, annealing	Annealing at 90 °C improved bonding diffusion	UTS ≈ 37.2 MPa	90 °C annealing, gyroid infill
Delbart et al. [72]	Nozzle dia., raster angle, LT	High crystallinity improved ductility > porosity effects	Strong crystallinity–toughness link	Larger nozzle, 45° raster
Popović et al. [73]	Nozzle temp, speed	Moderate heat + low speed optimised accuracy & bonding	Max tensile & lowest roughness at 190 °C, 40 mm/min	190 °C, 40 mm/min

Table 3. *Cont.*

Author	Parameters Studied	Cooling/Microstructure Effects	Mechanical Outcomes	Optimal Settings
Wang et al. [74]	Nozzle dia., bead width, infill orientation	Bead width dominated void geometry → flexural strength	Flexural strength ↑ 15% by bead width control	Wider beads at optimal width
Cadete et al. [75]	Speed, bed temp, nozzle temp, fan speed, flow	Slow speed + high bed temp promoted crystallinity	Crystallinity ≈ 71% (max)	10 mm/s, 80 °C bed
Gajjar et al. [76]	LT, raster angle, feed, nozzle temp	Thin layers + high temp ↓ voids, ↑ fusion	Strength ↑ 40% with raster optimisation	0.2 mm LT, 0° raster, 220 °C
Faizaan et al. [77]	Nozzle dia., LT	Large nozzle + fine layers ↓ porosity → strong bonding	CV ≈ 5.5% for tensile reproducibility	0.8 mm nozzle, 0.1 mm LT
Akhoundi & Jahanshahi [78]	Nozzle temp, extrusion width, LT, speed, infill	Zigzag infill + high temp improved inter-raster bonding	UTS ≈ 72 MPa	210 °C, 0.8 mm width, 0.3 mm LT, 80 mm/s
Kechagias et al. [79]	Flow rate, nozzle temp, speed	Heat input (flow, temp) governed fusion quality	Flexural ≈ 67 MPa; Surface Ra ≈ 13 µm	100% flow, 227 °C
Layeb et al. [80]	Nozzle temp, speed, LT, raster	Thin layers + 0° raster yielded strong bonding	UTS ≈ 51 MPa, E ≈ 3.4 GPa	210 °C, 30 mm/s, 0.1 mm LT, 0° raster

4.2. Acrylonitrile Butadiene Styrene (ABS)

Starting from 2019, Hibbert et al. [81] investigated the effect of build parameters and strain rate on the mechanical performance of ABS. Their factorial design considered raster angle, layer thickness, and fill style, and they found that orientation and thickness strongly affected strength and toughness. While the study clearly identified the parameters with the greatest impact, it did not extend to microstructural analysis. This omission limited their ability to connect mechanical changes to voids or interfacial bonding. Nevertheless, the results imply that the strong dependence of strength and toughness on raster orientation and layer thickness reflects how these parameters direct heat flow during deposition. Thinner layers and favourable raster alignments tend to retain heat longer, extending the time above T_g and enabling more robust interlayer fusion. Conversely, rapid cooling along certain orientations can create incomplete welds and promote anisotropy, explaining the sensitivity of their mechanical results to build setup.

A year later, Srinivasan et al. [82] explored tensile behaviour as a function of infill density, infill pattern, and layer thickness. They reported that denser infill and thinner layers consistently enhanced strength, while triangular infill patterns produced the most stable structures. The study was valuable in terms of mechanical modelling but limited by its lack of microstructural evidence. Nonetheless, their findings show that the superior strength at high infill densities and thin layers is consistent with slower internal cooling, as densely packed rasters restrict convective heat loss and prolong chain mobility. Increased thermal retention suppresses voids and encourages more effective interdiffusion across adjacent beads, which develops the overall mechanical features.

After that, in 2021, Rachman et al. [83] applied the Taguchi method to analyse the influence of layer height, infill pattern, and nozzle temperature on tensile strength. They found

that layer height and infill pattern were the dominant factors, while nozzle temperature played a secondary role. Although they did not include porosity or crystallinity data, the results indicate that the dominance of layer height and infill pattern on tensile behaviour can be interpreted through their effects on cooling uniformity. Thin layers deposit heat in smaller increments, enabling smoother thermal gradients and more consistent weld strength. Certain infill patterns also redistribute heat more evenly, avoiding abrupt cooling that limits molecular interpenetration. This enhanced thermal behaviour contributes directly to ABS weld development.

Additional ABS-focused work in 2021 by Nathaphan and Trutassanawin [84] broadened the parameter space by testing nozzle and bed temperatures, shell count, speed, and orientation. Their analysis showed that slower speeds and reduced layer height improved compressive strength, while elevated bed temperature enhanced interlayer bonding. Microscopy confirmed that porosity decreased when bed temperature was maintained above the glass transition. Also, Microstructural analysis links lower layer height to reduced porosity and stronger interlayer bonding, leading to enhanced compressive strength. The limitation was that tensile behaviour was not studied, but the results still strongly demonstrated that the enhancements in compressive strength under slow speeds, low layer heights, and elevated bed temperature demonstrate how maintaining the printed polymer near or slightly above T_g improves bonding. Higher bed temperatures reduce the interlayer thermal shock that otherwise causes premature solidification, residual stresses, and porosity. Their microscopy images clearly show that controlling cooling gradients is central to reducing void entrapment in ABS.

In the next year, Abbas et al. [85] studied compressive behaviour under variations in shell width, infill density, infill pattern, and layer thickness. They found that infill density and shell width were the most influential factors, with thinner layers supporting stronger adhesion. However, no microscopy was provided to validate the presence or absence of voids. Even so, the influence of shell width and infill density on compressive behaviour suggests that thermal mass effects dictate interlayer cohesion: wider shells and dense infills store heat longer, delaying cooling and improving fusion. Thin layers also reduce thermal discontinuities between successive rasters. Even without microscopy, their mechanical trends strongly imply cooling-rate-mediated weld strengthening.

Also in 2023, Ahmad and Yahya [86] investigated tensile properties under different infill patterns, raster orientations, layer thicknesses, and print speeds. They showed that certain raster orientations improved both strength and modulus, especially when combined with appropriate thickness values. Microscopy confirmed denser interlayer contact and fewer voids under these conditions. The study was somewhat limited in scope, but their improvements in strength and stiffness under certain raster orientations and layer settings reflect that the optimized parameter combination had assisted filaments in packing more tightly and bonding more effectively. Because when neighbouring strands stay warm for longer, the heat from each new pass allows more time for the layers to fuse. In contrast, when strands cool too quickly or are placed far apart, the chains cannot move enough to close gaps, leaving more voids. The micrographs clearly show how these cooling effects influence interlayer bonding and overall part quality.

Another 2023 study by Yankin et al. [87] compared ABS and nylon under variations in infill density, pattern, and speed. They identified infill density as the most dominant factor for mechanical performance, with higher-density prints consistently outperforming lower-density ones, as Figure 12 shows. Although the study did not include microstructural analysis, its results still strongly demonstrate that infill density strongly influences both ABS and nylon, suggesting that the amount of deposited material controls how well heat is retained in the part. Higher densities hold warmth longer, preventing the weld

interface from solidifying too quickly and reducing interlayer defects. The resulting mechanical behaviour reflects a more thermally stable bonding zone, with cooling occurring more gradually.

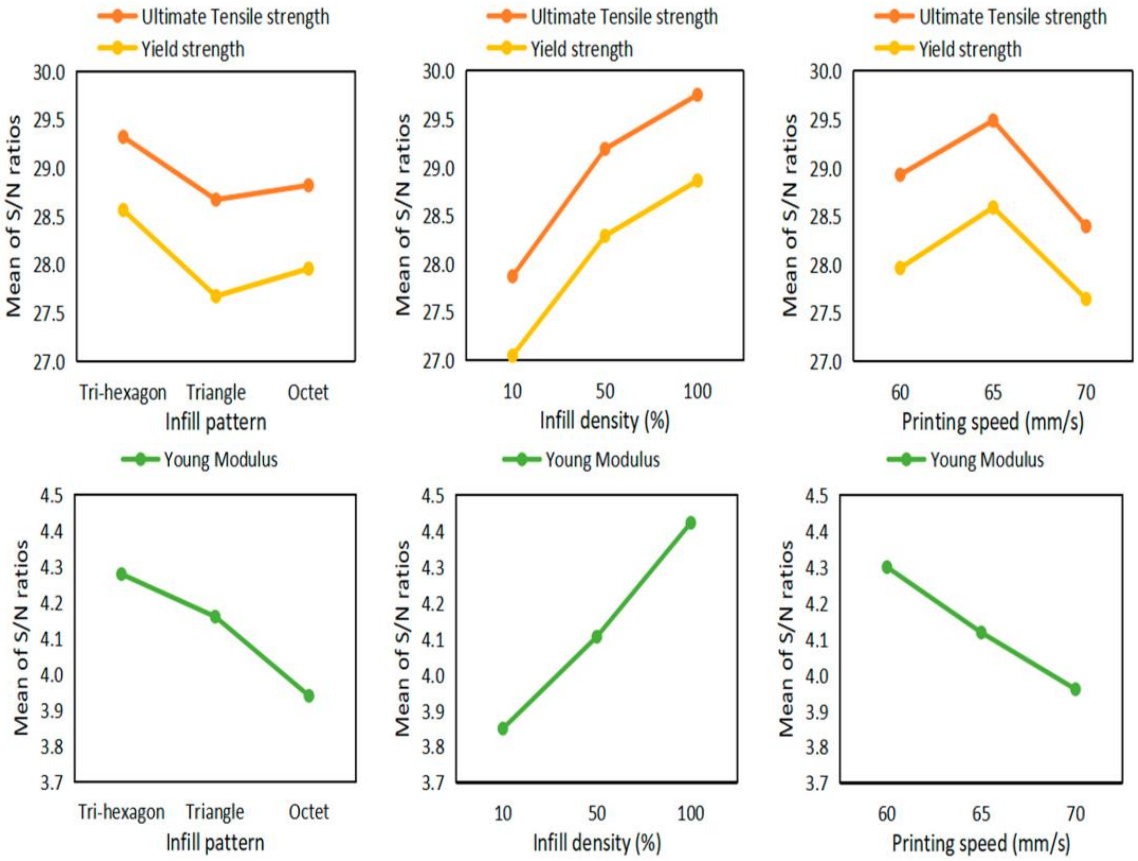


Figure 12. (S/N) ratio analysis of ABS specimens under tensile loading [87].

In the same year, Mushtaq et al. [88] adopted RSM to optimise multiple objectives, including strength, surface quality, and energy efficiency. They showed that infill density was most significant for mechanical performance, while layer thickness and speed balanced surface quality and print time. Microscopy revealed that denser infill reduced porosity and enhanced interlayer bonding, though very thin layers also increased brittleness. While crystallinity was not addressed, the reduced porosity observed at high infill densities and optimal layer thicknesses arises from smoother cooling transitions that prevent early solidification at the interface. However, their note on excessive brittleness at very thin layers reflects a secondary thermal effect where overly thin layers may crystallize or stiffen too quickly after fusion, limiting ductility. This duality shows the need for balanced cooling conditions in ABS.

Later, a year ago, Khodaee et al. [89] studied multi-material ABS/PLA composites, focusing on tensile and flexural behaviour. They reported that high infill density and a 0° raster orientation produced the strongest specimens. Microscopy confirmed improved adhesion and reduced porosity under these conditions. Although the study did not examine nozzle or bed temperature, the findings reinforce that dense infill and favourable orientation enhance the thermal homogeneity of the multi-material ABS/PLA interface, enabling longer durations of chain mobility before solidification. This mitigates mismatched cooling shrinkage between the two polymers, which otherwise induces porosity and weak adhesion. Their microscopy findings confirm that deposition density effectively moderates cooling-induced interfacial stresses.

To synthesize the effects of process parameters on cooling dynamics, microstructural evolution, and mechanical performance in ABS, Table 4 provides a comparative overview of previously reported experimental studies, correlating processing conditions with cooling-induced microstructural features, interlayer bonding quality, and the resulting mechanical responses, together with the optimal parameter combinations identified in the literature.

Table 4. Comparative summary of ABS studies.

Author	Parameters Studied	Cooling/Microstructure Effects	Mechanical Outcomes	Optimal Settings
Hibbert et al. [81]	Raster angle, layer thickness, fill style	Thicker layers altered cooling, residual stress, bonding	Modulus of toughness ↑; UTS ≈ 27.4 MPa	0.254 mm LT, [0°/90°] raster, solid fill
Srinivasan et al. [82]	Infill pattern, infill density, LT	Dense infill slowed cooling, reduced air gaps	Max tensile strength with triangular infill	Triangular infill, high density, thin LT
Rachman et al. [83]	LT, infill pattern, nozzle temp	Thinner layers improved heat distribution & bonding	Highest tensile strength at 0.2 mm LT	0.2 mm LT, line infill, 230 °C nozzle
Nathaphan & Trutassanawin [84]	Nozzle temp, bed temp, shells, LT, speed, orientation	Elevated bed temp slowed cooling, enhanced bonding	Max compressive stress at low LT, low speed	0.20 mm LT, 41–50 mm/s, 109–120 °C bed
Abbas et al. [85]	Shell width, infill density, pattern, LT	Dense infill & thin layers moderated cooling, reduced voids	Compressive strength ↑ at 60% infill	0.8 mm shell, 60% infill, 0.2 mm LT
Ahmad & Yahya [86]	Infill pattern, raster orientation, LT, speed	Orientation controlled cooling paths, reducing voids	45° raster & 0.3 mm LT gave highest UTS	45° raster, 0.3 mm LT, normal speed
Yankin et al. [87]	Infill pattern, density, speed	Dense triangular infill retained heat, ↓ porosity	Max tensile at 100% density, tri-hex infill	100% infill, tri-hex pattern, 65 mm/s
Mushtaq et al. [88]	LT, infill density, speed	High infill slowed cooling, reduced porosity	Optimal multi-objective performance at high density	0.27 mm LT, 84% infill, 51 mm/s
Khodaee et al. [89]	Infill density, raster angle, speed	Dense infill & 0° raster promoted uniform cooling & bonding	Max tensile & flexural strength	100% infill, 0° raster, 26 mm/s

4.3. Other Polymers

In 2019, Ding et al. [90] investigated high-performance polymers PEEK and PEI, examining how nozzle temperature and build orientation affected porosity and flexural behaviour. Their results showed that increased nozzle temperatures enhanced interlayer bonding and reduced porosity, particularly for PEEK, while horizontal orientation yielded superior flexural strength. The improved bonding and reduced porosity at higher nozzle temperatures reflect the strong influence of thermal mass and cooling rate on semi-crystalline PEEK and amorphous PEI. Elevated deposition temperatures slow down solidi-

fication, allowing deeper diffusion and suppressing micro-void formation. The superior flexural performance in horizontal orientations further indicates that these geometries retain heat more effectively, reducing steep cooling gradients that would otherwise weaken the interlayer interface.

In 2020, Ajay Kumar et al. [91] studied carbon-fibre reinforced PETG composites, evaluating tensile, flexural, and hardness properties under different processing conditions using a Box–Behnken design. Parameters included print speed, infill density, and layer thickness. They found that fibre reinforcement enhanced mechanical performance, while parameter selection influenced anisotropy. Although microstructural evidence was limited, their reported improvements in mechanical behaviour under optimized printing parameters correspond to a more controlled cooling profile in the fibre–matrix system. Slower cooling promotes improved wetting of fibres by the PETG matrix, decreasing interfacial voids and enhancing load transfer. In contrast, rapid cooling restricts matrix relaxation around fibres, trapping defects that contribute to anisotropy. The observed performance trends align with well-established composite cooling-rate effects.

In the same year, Zhao et al. [92] examined PAPC-II composite bone scaffolds fabricated by ME with multiple parameters, including flow rate, layer thickness, infill density, shell number, speed, and raster angle. Their analysis revealed that scaffold porosity and mechanical properties were strongly influenced by printing conditions, particularly extrusion temperature. While the work was largely biomedical in focus, it highlighted that the enhanced compressive behaviour under elevated extrusion temperatures reflects a thermally moderated deposition process, where delayed cooling improves pore uniformity and reduces internal stress concentration. Slow cooling also prevents abrupt solidification of scaffold struts, leading to more consistent mechanical properties. Their work shows how cooling behaviour is integral to both structural integrity and biomedical functionality in porous scaffolds.

In 2021, the study by Zhang et al. [93] investigated the optimization of 3D printed Nylon 618 spur gears' dynamic performance and wear resistance, using a genetic algorithm-based artificial neural network for multi-parameter regression. The authors examined how printing temperature, speed, bed temperature, and infill affect gear strength and wear life, finding that these parameters play a key role in durability and bonding. Infill, speed, and temperature were especially important for material strength, while Nylon 618 showed superior heat resistance and toughness due to its structure and layer adhesion. However, not all parameter interactions were fully explored. However, they demonstrated that the sensitivity of wear resistance and dynamic performance to print temperature and speed is closely linked to the thermal history of the nylon layers. Higher temperatures extend the molten lifetime of the deposited strands, enabling more complete fusion and reducing interlayer stress concentrations that initiate wear. on the other hand, rapid cooling restricts polymer relaxation and produces brittle interfaces that accelerate surface fatigue.

Also in 2021, the study by Vaes et al. [94] addresses weak interlayer bonding in semi-crystalline nylon copolymers by examining how thermal history and crystallinity interact with strength development. They varied head and bed temperatures, printing speed, and nylon type, finding that higher printing temperatures improved bonding but excessive crystallinity reduced ductility and limited chain interdiffusion. Additionally, elevated bed temperatures increased crystal formation while restricting interlayer mobility. Although porosity was not deeply analyzed, the interplay they observed between crystallinity, ductility, and bonding strength arises from how cooling rate shapes the semi-crystalline morphology. Slow cooling promotes larger, more stable crystals but restricts interlayer diffusion, while faster cooling preserves amorphous regions that favour welding but reduce stiffness.

Their results illustrate the delicate balance needed between crystallization kinetics and weld mobility to optimize nylon performance.

The same year, Hsueh et al. [95] investigated the impact of printing temperature and speed on the mechanical and thermal properties of PLA and PETG in FDM to identify optimal conditions. By varying these two parameters and testing material strength and thermal deformation, they found that higher temperatures improved layer fusion and reduced gaps. As Figure 13 shows, PLA was generally stronger, while PETG had better heat resistance, with optimal bonding achieved through proper temperature and speed selection. The findings suggest that the improved layer fusion at high printing temperatures and low speeds is attributable to extended thermal exposure, which delays cooling and enables more complete wetting between layers. Their comparison also shows that PETG, with slower crystallization kinetics, remains sensitive to rapid cooling that limits interfacial healing. The differences in strength between PLA and PETG directly mirror the distinct thermal responses of the two polymers.

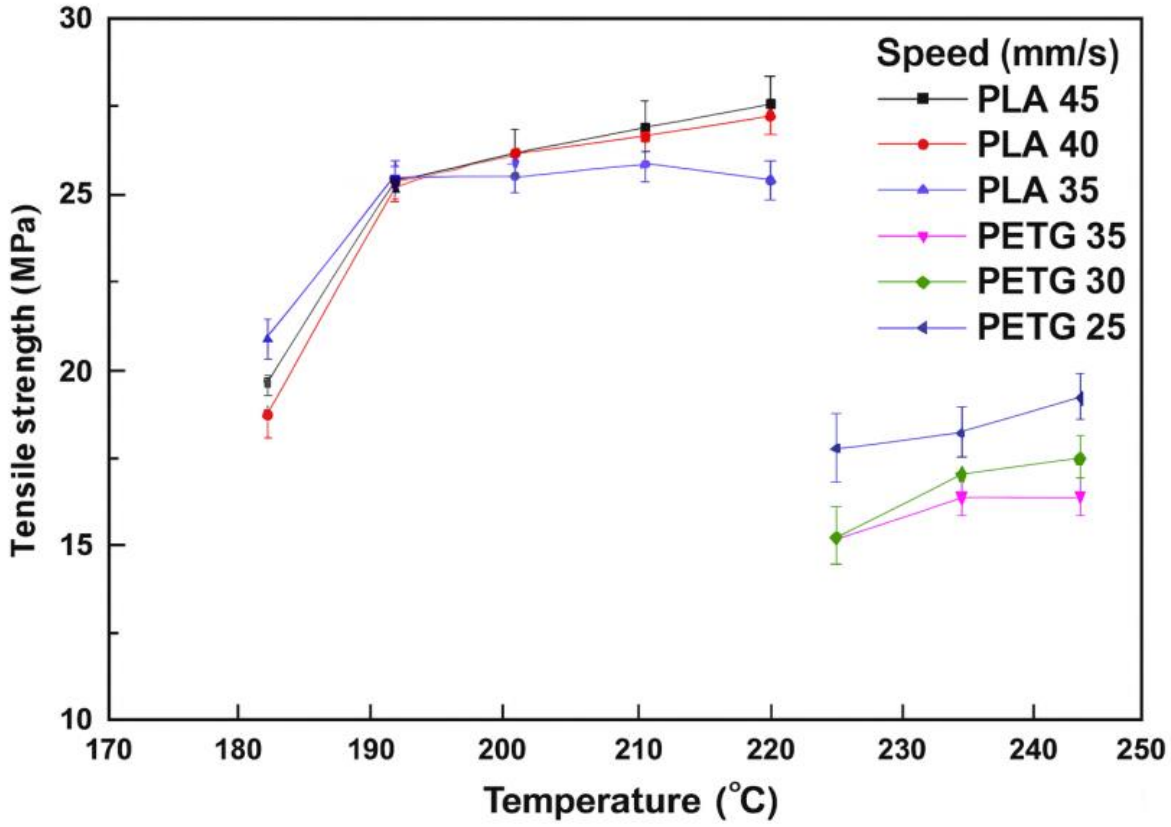


Figure 13. Effect of Nozzle Temperature on the Tensile Strength [95].

In 2022, the study by Vamshinath et al. [96] examines the mechanical performance and failure behaviour of adhesively bonded single lap joints (SLJs) in FDM 3D-printed PETG, focusing on joint strength optimization. Different raster angles, raster widths, and layer thicknesses have affected bond performance, with certain setups yielding stronger joints and most failures occurring within the adhesive bond itself. While crystallinity and porosity were not directly analyzed, deposition methods influenced layer adhesion. It is clear that the cooling rate during printing impacts layer fusion, which indirectly affects interfacial adhesion and mechanical performance.

Also same year, the study by Sikder et al. [97] tackled the challenge of optimizing FDM for PEEK to match conventional mechanical properties for high-performance use. By adjusting nozzle and chamber temperature, layer height, and speed, they found that higher

temperatures and smaller layer heights improved bonding and microstructure, with annealing enhancing crystallinity and mechanical strength. Crystallinity influences interlayer bonding, while porosity from printing gaps initiates micro-cracks, reducing strength. The improvements seen at high nozzle and chamber temperatures demonstrate that effective PEEK printing relies heavily on minimizing cooling-induced crystallinity gradients. Small layer heights maintain heat within adjacent rasters, reducing abrupt crystallization that weakens interlayer adhesion. Their annealing results further illustrate that reheating can correct cooling-rate-induced defects by enabling more uniform crystal development.

A year later, the study by Padhy et al. [98] focused on optimizing ME process parameters for PEEK using an Ensembled Surrogate-Assisted Evolutionary Algorithm (SAEA). By adjusting layer height, print speed, direction, and nozzle temperature, the study identified that print direction strongly affects crystallinity, strength, and surface quality, while continuous optimization improves outcomes over conventional methods. Limitations included discrete experimental levels and decolourization linked to amorphous crystals at low nozzle temperatures. The study's robust methodology underscores that the strong influence of print direction on crystallinity and strength reflects how directional heat flow governs cooling behaviour. Certain directions promote slower cooling and more favourable crystal structures, while others force steep temperature drops that limit diffusion and produce amorphous–crystalline mismatch at the interface.

Another 2023 study by Hua et al. [99] explored mechanical performance in 3D-printed short basalt fibre-reinforced polyamide using FDM, focusing on printing temperature, speed, and layer height. Taguchi design and mechanical tests showed major gains from higher temperatures and lower layer heights, which reduced voids and improved interlayer bonding. Printing temperature had the largest effect, while speed was less influential. Results show that the reduced voids at high print temperatures and low layer heights indicate a prolonged molten state that improves fibre–matrix adhesion. Whereas rapid cooling under less favourable conditions traps interfacial defects and limits stress transfer efficiency. Therefore, regulating cooling during printing improves fibre–matrix bonding and microstructural quality.

Finally, Gómez-Ortega et al. [100] in 2024 examined wall thickness, infill percentage, and nozzle temperature in carbon fibre-reinforced nylon composites. Infill percentage and wall thickness primarily drove tensile and flexural strength, but excessive infill led to internal voids and crack growth at interfaces. Balanced parameters were needed for optimal structure. These findings highlight that the mechanical trends associated with infill percentage and wall thickness reflect how thermal mass determines cooling rate in composite systems. Thick walls and dense infill slow cooling, enabling better matrix relaxation and stronger fibre–matrix integration. Excessively dense infill, however, can generate internal thermal gradients that promote crack initiation once cooling eventually occurs, demonstrating the need for balanced heat dissipation.

To synthesize the effects of process parameters on cooling dynamics, microstructural evolution, and mechanical performance in other polymers, Table 5 provides a comparative overview of previously reported experimental studies, correlating processing conditions with cooling-induced microstructural features, interlayer bonding quality, and the resulting mechanical responses, together with the optimal parameter combinations identified in the literature.

Table 5. Comparative summary of Other Polymer studies.

Author	Material	Parameters Studied	Cooling/Microstructure Effects	Mechanical Outcomes	Optimal Settings
Ding et al. [90]	PEEK, PEI	Nozzle temp, orientation	High temp slowed cooling, ↓ porosity, ↑ bonding	PEEK: Flexural ≈ 135 MPa; Density ≈ 92.8%	390–400 °C nozzle, horizontal
Ajay Kumar et al. [91]	PETG-CF	Speed, infill density, LT	Dense infill slowed cooling, improved fibre bonding	Tensile, flexural, hardness improved	60 mm/s, 80% infill, 0.2 mm LT
Zhao et al. [92]	PAPC-II	Flow, LT, infill, shell, speed, raster	High flow & density slowed cooling, reduced voids	Tensile ≈ 140 MPa; Yield stress ≈ 115 MPa	125% flow, 0.25 mm LT, 90% infill
Zhang et al. [93]	Nylon 618	Temp, speed, bed temp, infill	Crystallinity ↑ → wear resistance; but ↓ bond strength	Fatigue life up to ≈52 h	250 °C, 70 mm/s, 80% infill
Vaes et al. [94]	Nylon copolymers	Liquefier temp, bed temp, speed	High crystallinity restricted diffusion, ↓ bond strength	Tear energy ↑ at 260 °C but weld weak	260 °C nozzle, 110 °C bed
Hsueh et al. [95]	PLA, PETG	Temp, speed	High temp ↑ fusion, ↓ porosity	PLA > PETG in strength; PETG > PLA in thermal resistance	High temp + high speed (PLA)
Vamshinath et al. [96]	PETG joints	Raster angle, raster width, LT, adhesive thickness	Raster alignment & thin LT improved adhesion	Tensile ≈ 61 MPa, high stiffness	0° raster, 1 mm width, 0.2 mm LT
Sikder et al. [97]	PEEK	Nozzle, bed, chamber temp, LT, speed	High nozzle & chamber temps ↑ crystallinity, ↓ voids	Tensile, flexural, compressive improved	410 °C nozzle, 90 °C chamber
Padhy et al. [98]	PEEK	LT, speed, orientation, nozzle temp	Orientation & temp controlled cooling, crystallinity	UTS up to ≈97.8 MPa; Elongation up to ≈121%	0.1 mm LT, 16 mm/s, 401 °C nozzle
Hua et al. [99]	BF–Polyamide	Temp, speed, LT	High temp & fine layers ↓ voids, ↑ fibre adhesion	Tensile ≈ 36.7 MPa; Compression ≈ 30.6 MPa	215 °C, 35 mm/s, 0.2 mm LT
Gómez-Ortega et al. [100]	PA-CF	Wall thickness, infill %, nozzle temp	High infill ↑ bonding but risked voids	Tensile ≈ 52.8 MPa; Modulus ≈ 1366 MPa	99% infill, 1.2 mm wall, 230 °C nozzle

5. Cooling Rate Mechanism & Quantitative Characterization Methods

Quantifying cooling rate in ME is central to linking process parameters with thermal history, interlayer weld formation, crystallization behaviour, and defect evolution in both amorphous and semi-crystalline polymers. A rigorous treatment requires not only qualitative descriptions but also quantitative cooling rate data, explicit structure property relationships, and a clear overview of in situ measurement methodologies [30,33,94].

Quantitative cooling rates during FDM printing vary significantly depending on the choice of polymer and process parameters [33,94]. In ME, the cooling mechanism follows a dual-phase thermal trajectory, rapid interfacial cooling followed by controlled bulk cooling. The rapid interface cooling phase begins immediately after extrusion, when the molten filament contacts a cooler underlying layer. This produces steep thermal gradients and cooling rates of 50–100 °C/s for PLA, tens of °C/s for PA12 and ABS, and 40–50 °C/s or higher for PEEK. Over a brief few-seconds window, the interface temperature remains above the polymer's T_g (≈60 °C for PLA, 50 °C for PA12, 106 °C for ABS, 143 °C

for PEEK), allowing adequate chain diffusion and weld formation [33,94,97]. Although this rapid quench primarily arises from the hot–cold layer contact, it may be intensified by auxiliary cooling, particularly part-fan use in PLA printing. After that, once weld formation stabilizes, the process transitions into the bulk cooling phase, where the entire part cools more gradually at 1–10 °C/s [45,50,60,94]. This moderated cooling reduces thermal gradients, limits warping, and prevents excessive residual stress [41,43,47]. In PLA, it governs crystallinity and dimensional stability; in PA12, it balances crystallization with mechanical performance. In ABS, it mitigates warping, often aided by heated beds and limited fan use. In PEEK, slower post-interface cooling promotes crystallinity while reducing internal stresses [41,43,90,94,97].

Robust analysis of cooling behaviour in ME relies on quantitative in situ temperature measurement, primarily via embedded thermocouples and infrared (IR) thermography, which offer complementary strengths [30–32].

- **Embedded thermocouples:** They are positioned at the part/bed interface or between designated layers to record local time–temperature histories throughout the build. By capturing the full heating–cooling cycle—including reheating from subsequent layer deposition—they provide direct insight into thermal gradients, melt reheating behaviour, and layer-wise cooling rates. Such measurements have reported cooling rates ranging from only a few °C/s to hundreds of °C/s in polymer-quenching and material-extrusion studies [30,94]. However, several limitations affect accuracy. Thermocouples have a finite response time (typically 100–140 ms), which can smear rapid thermal transients. Reliable measurements also require excellent thermal contact with the surrounding polymer; any voids or incomplete bonding can insulate the junction, causing systematic underestimation of true cooling rates. Additionally, the sensor's physical presence may disturb the local thermal field, especially in small features or thin layers, introducing further uncertainty into the captured data [30–32].
- **Infrared Thermography:** IR thermography offers non-contact, full-field temperature measurements with frame rates in the tens of hertz and spatial resolution below 100 µm, enabling direct visualization of weld-zone temperatures, surface cooling rates, and spatial thermal gradients during extrusion. Because IR cameras detect radiated energy rather than true temperature, accurate use requires careful handling of surface emissivity, mitigation of reflections from nearby hot components, and calibration against reference temperatures to convert raw signals into reliable thermal fields [31,32]. IR approaches are especially valuable for revealing the spatial heterogeneity of cooling, capturing phenomena such as asymmetric heat dissipation, cooling fronts, and thermally influenced defect formation [30,94].

When combined, these methods provide a comprehensive thermal characterisation framework in FDM, where point-level precision from embedded sensors is complemented by surface-level thermal mapping from IR imaging, enabling more robust validation of thermal models and deeper understanding of interlayer bonding mechanisms [30–32].

6. Critical Analysis and Discussion

Recent advances in FDM research have highlighted that process optimization is inseparable from the underlying thermal environment in which deposition occurs. While conventional studies often focus on discrete parameters such as nozzle temperature, speed, or layer thickness, these variables only serve as proxies for more fundamental thermal histories—specifically, how long deposited filaments remain above the coalescence temperature, the steepness of thermal gradients between adjacent layers, and the rate at which heat dissipates into the environment.

For semi-crystalline PLA, this thermal history directly dictates crystallinity and interlayer adhesion. When deposition cools too rapidly, crystallization occurs prematurely, restricting molecular mobility and limiting chain entanglement across layers. Conversely, prolonged exposure above the glass transition enables interdiffusion and stronger bonding. Luzanin et al. [62] and Von Windheim et al. [66] demonstrated that high nozzle temperature and slow printing speed improve diffusion, yet Perez et al. [101] provided more definitive evidence by coupling mechanical testing with heat-transfer simulation. Their work showed that interlayer strength correlates more strongly with interface temperature evolution than with nominal print settings, underscoring the need to interpret optimization in thermal rather than purely parametric terms.

In amorphous ABS, the absence of crystallization shifts the thermal challenge toward residual stresses and warping. Thermal gradients created by non-uniform cooling induce internal strain, which manifests as delamination or dimensional distortion. Although raster orientation and infill density contribute to stress distribution, Ahmad and Yahya [86] and Mushtaq et al. [88] observed that mechanical anisotropy persists when cooling is uncontrolled. This reflects the broader reality that mechanical anisotropy originates thermally, with insufficient control over interlayer temperature homogenization.

Emerging solutions highlight the importance of real-time monitoring and active thermal management. Fu et al. [102] reviewed in situ monitoring approaches and emphasized that thermocouples and infrared imaging, though feasible, remain underutilized in routine optimization studies. Kishore et al. [103] demonstrated that infrared preheating significantly improves interlayer fusion in large-scale additive manufacturing by extending the bonding window, as Figure 14 shows. While Hossain et al. [104] showed that IR thermography enables real-time defect detection, making it possible to correlate porosity formation with thermal irregularities. Extending this approach, McBean et al. [105] applied in-process monitoring to high-temperature polymers, illustrating that robust measurement of layer temperature is essential for reproducibility. Whereas Baqasah et al. [106] further demonstrated that dynamic response monitoring of ABS under thermomechanical loads enables in situ quantification of damage and stiffness reduction, validating the necessity of integrated real-time diagnostics.

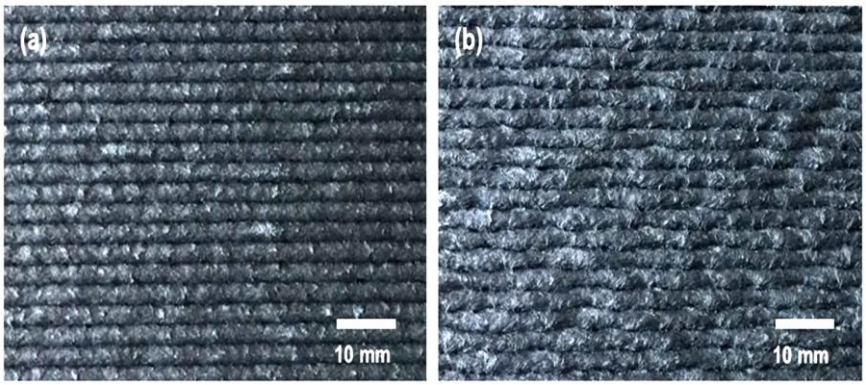


Figure 14. SEM images (**a**) show the effect of heating by IR on layers, and (**b**) No IR heating [102].

Collectively, these works point to a paradigm where thermal validation becomes as essential as mechanical testing in defining optimal FDM conditions. Omer et al. [107] further reinforce this by synthesizing the latest advances and highlighting the inadequacy of purely parametric optimization without thermal grounding. Also, Khan et al. [108] introduced a non-destructive monitoring approach using material fundamental frequency measurement to track fatigue progression and estimate remaining life. This concept of integrating real-time mechanical diagnostics aligns with the need for adaptive process

control in manufacturing, where understanding thermal and mechanical degradation can lead to improved part reliability and performance.

Taken together, the literature reveals that much of the progress in PLA and ABS optimization can be reinterpreted as the management or mismanagement of heat. Thermal gradients, cooling rates, and diffusion windows remain the invisible variables underlying porosity, anisotropy, and residual stress. A critical shortcoming is that relatively few studies explicitly measure or model these phenomena, leaving many reported optimizations system-specific and difficult to generalize.

7. Challenges in FDM Process Optimization

Although parameter tuning has yielded improvements, several challenges persist, each with a clear thermal origin.

Thermal gradients represent the most fundamental challenge in the ME process [109]. Each new layer cools rapidly in ambient conditions while underlying layers retain residual heat, creating steep intra- and interlayer temperature differences. Luzanin et al. [62] and Sikder et al. [97] showed that such gradients influence crystallization and bonding, while Mushtaq et al. [88] linked them to dimensional instability in ABS. Yet few works quantify these gradients experimentally, leaving the mechanisms only partially understood.

Interlayer bonding deficiencies continue to undermine structural reliability. While increasing nozzle temperature can improve diffusion [71], the lack of thermal control between layers makes it difficult to achieve uniform bonding throughout the print [110]. Although optimized raster orientations can distribute loads more effectively, true z-direction strength depends on maintaining sufficient thermal overlap between layers. Perez et al. [101] confirmed that poor interface temperature histories, rather than geometry alone, dictate bonding strength. Even post-processing strategies such as annealing fail to erase discontinuities when initial fusion is incomplete [66]. Kishore et al. [103] showed that controlled IR preheating can directly address this by extending interlayer bonding time, but such strategies are rarely adopted in standard practice.

Void formation and porosity remain endemic, particularly at bead junctions and infill-wall transitions. These features reflect localized cooling and insufficient thermal bridging. Gómez-Ortega et al. [100] found void clustering in composites, while Hossain et al. [104] demonstrated that IR thermography can visualize these defects during printing. Despite such advances, routine optimization continues to treat voids as geometric byproducts rather than thermally induced failures.

Finally, residual stress poses long-term challenges. In PLA, stress interferes with crystallinity, while in ABS and PEEK it induces warping and dimensional distortion. McBean et al. [105] highlighted that even high-temperature polymers suffer stress accumulation if cooling is uncontrolled, emphasizing the universality of this challenge. Similarly, Khan [108] demonstrated that elevated thermal exposure accelerates fatigue damage in aluminium alloys by destabilizing the microstructure and reducing mechanical endurance, reinforcing the broader link between thermal stress and structural degradation. Given the higher thermal sensitivity and viscoelastic nature of polymers, such effects are expected to be even more pronounced in ME-processed materials. Yet, residual stress measurement remains underrepresented in the literature, with most studies relying on static tensile tests rather than stress analysis or basic stress analyses that offer limited insight into the actual residual stresses, as shown in Figure 15 [111].

In short, each of the major barriers (gradients, bonding deficiencies, porosity, residual stress) stems from inadequate thermal control, highlighting the need for real-time thermal monitoring, better heat control systems, and predictive modelling of thermal and stress behaviour [112].

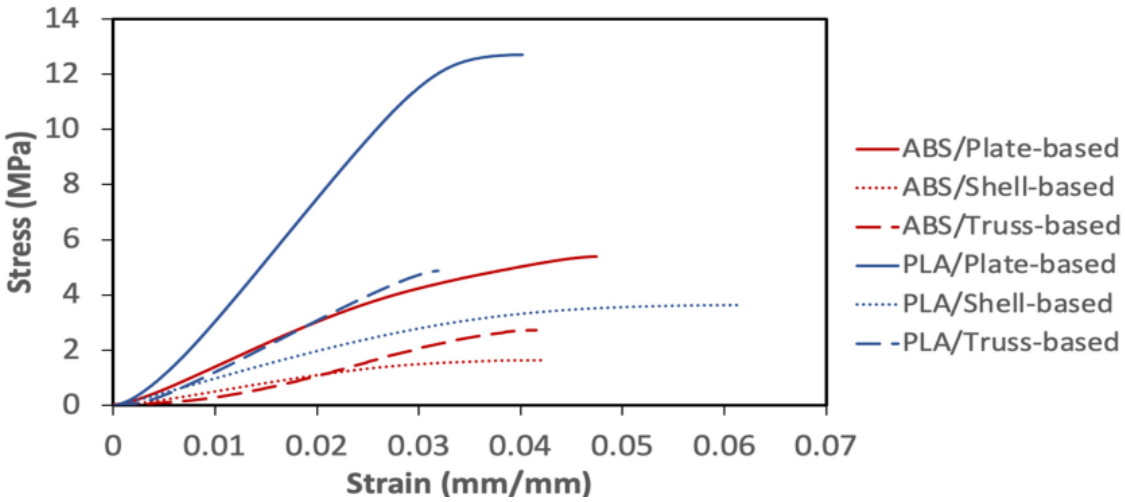


Figure 15. The stress–strain curve provides the mechanical behaviour of the samples and could help to find a microstructural design and properties [113].

8. Gaps and Suggested Future Work

Despite considerable advances in FDM process optimisation, several significant research gaps remain unaddressed, offering opportunities for future investigation.

A common shortcoming across many studies is the isolated examination of individual parameters rather than holistic multi-variable interactions. Most experimental designs (such as one-factor-at-a-time (OFAT) or basic Taguchi methods) fail to capture the synergistic effects between critical factors like nozzle temperature, print speed, layer height, raster orientation, and infill density. Consequently, optimal settings determined under narrow constraints often do not generalise across different geometries, materials, or machines. Recent work by Perez et al. [101] illustrates how integrating heat-transfer simulations with mechanical testing can better capture these interactions, reinforcing that thermally informed frameworks are necessary to overcome the limitations of purely parametric optimisation.

Furthermore, thermal management during printing remains insufficiently controlled or monitored in real-time. Although some studies introduced thermal imaging and simulation to reveal steep temperature gradients, very few practical systems incorporate real-time temperature feedback for dynamic control [114]. This lack of in situ regulation continues to result in unpredictable crystallinity, residual stress, and bonding inconsistencies, particularly for high-performance polymers. Reviews by Fu et al. [102] highlight that infrared thermography and thermocouples offer feasible solutions, while more recent advances by Hossain et al. [104] demonstrate that IR sensing can also support real-time defect detection. Despite these advances, such techniques remain underutilised, limiting their impact on reproducibility.

Another underexplored area is the long-term behaviour of FDM-printed components under operational or environmental loading. While many studies report static tensile or flexural strength, there is minimal investigation into fatigue behaviour, creep resistance, or structural degradation over time, especially in humid or high-temperature settings. These omissions limit the applicability of FDM parts for functional end-use or structural roles in industrial settings. McBean et al. [105] showed that in-process thermal monitoring improves reproducibility in high-temperature polymers, yet stress evolution remains poorly characterised. More advanced diagnostics such as digital image correlation or neutron diffraction could close this gap.

Additionally, there is a scarcity of optimisation frameworks that incorporate machine learning (ML) or artificial intelligence (AI). Only a few recent studies have started

leveraging ML for parameter prediction or surrogate modelling, yet the vast parameter space and variability across machines, materials, and geometries make this a promising direction. Data-driven models can reduce experimental burden and enable real-time adaptive printing [115]. Crucially, ML approaches should integrate thermal data as input variables, ensuring that predictions capture not only geometric but also thermal–mechanical couplings.

In terms of sustainability and material development, the majority of current research remains confined to commercial PLA and ABS filaments. More studies should evaluate bio-based, recycled, or composite materials under the same optimisation protocols, while also assessing recyclability, environmental ageing, and performance consistency. Baqasah et al. [106] stress that this gap in material diversity, especially regarding how new materials alter thermal conductivity and crystallisation behaviour, must be addressed if ME is to mature into a sustainable technology. Additionally, multi-material ME remains insufficiently explored in the context of cooling-rate behaviour. Differences in thermal conductivity, heat capacity, and crystallization kinetics between adjacent polymers can generate heterogeneous cooling profiles and interfacial temperature gradients. Future work should therefore investigate how these mismatched thermal properties affect interlayer diffusion, bonding quality, and the structural reliability of multi-material components.

Finally, strategies for active thermal control remain underexplored in standard practice. While chamber heating and print-enclosure strategies are sometimes applied, they are rarely optimised alongside parameters. Work by Kishore et al. [103] demonstrated that IR preheating can significantly extend interlayer bonding time and improve mechanical strength, yet this remains an isolated demonstration. Broader integration of preheating, local reheating, and adaptive chamber control into optimisation frameworks represents a major opportunity for future work.

In conclusion, the path forward lies not in isolated parameter tuning but in frameworks that unify parameter optimisation with thermal validation, in situ monitoring, predictive modelling, and sustainability considerations. Closing these gaps will enable the reproducibility, scalability, and industrial reliability that FDM still lacks (Figure 16).

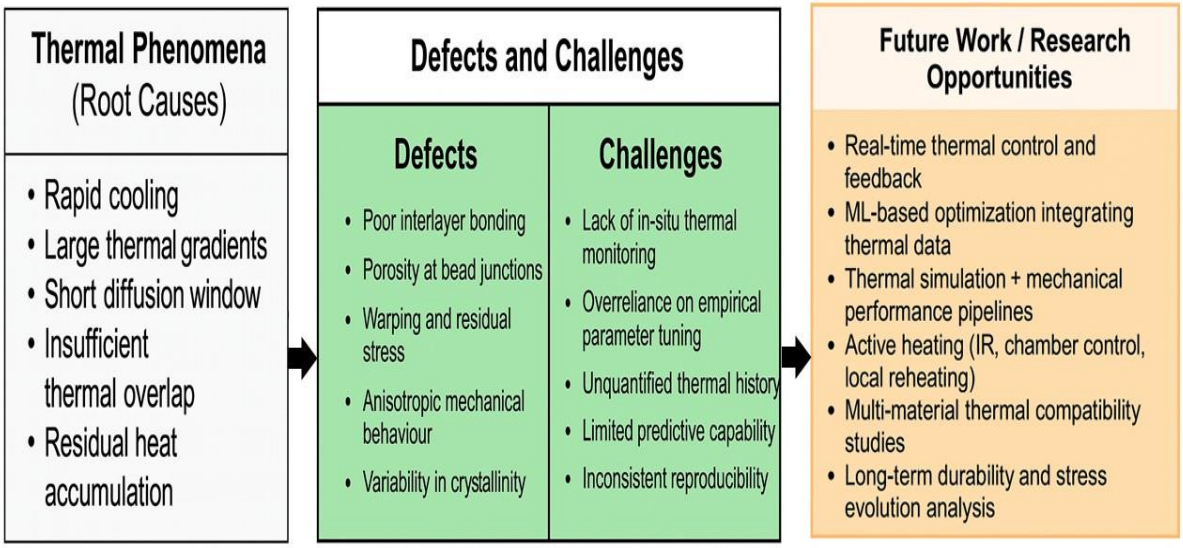


Figure 16. Overview of thermal phenomena discussion, resulting defects and challenges, and future research opportunities in FDM process optimisation.

9. Conclusions

This review demonstrates that cooling rate is the central thermodynamic variable governing the thermal history and, consequently, the microstructural and mechanical

performance of ME-fabricated polymers. The analysis shows how key process parameters, material properties, and heat-transfer mechanisms collectively dictate cooling behaviour, and how this behaviour mediates crystallinity development, interlayer bonding, defect formation, and residual stress. Existing optimization studies were reinterpreted through a cooling-rate-centred framework, highlighting both the progress made and the limitations of current empirical approaches. Persistent challenges—including insufficient thermal monitoring, limited predictive modelling, and the lack of standardized methods to quantify cooling rate—continue to constrain reliable process optimization. Therefore, advancing ME requires more rigorous thermal characterization, improved modelling tools, and process-parameter strategies that explicitly target control of cooling rate.

By framing cooling rate as an active design variable rather than a passive outcome, future research can establish more precise process control and more reliable predictions of part quality. This shift will not only refine the reliability and precision of ME but also accelerate its integration into high-performance applications across aerospace, biomedical, and structural engineering domains.

Author Contributions: Conceptualization, A.S.A. and M.K.; methodology, A.S.A. and M.K.; formal analysis, A.S.A. and M.K.; investigation, A.S.A.; resources, A.S.A.; data curation, A.S.A.; writing—original draft preparation, A.S.A.; writing—review and editing, A.S.A.; visualization, A.S.A.; technical, A.S.A.; supervision, M.K. and F.H.; project administration, A.S.A. All authors have read and agreed to the published version of the manuscript.

Funding: This research received no external funding.

Data Availability Statement: The original contributions presented in this study are included in the article. Further inquiries can be directed to the corresponding author.

Acknowledgments: Sincere appreciation is extended to the Deanship of Scientific Research at Al-Baha University.

Conflicts of Interest: The authors declare no conflicts of interest.

Declaration of Generative AI and AI-Assisted Technologies in the Manuscript Preparation Process: During the preparation of this work, the author(s) used [Mendeley, Grammarly] in order to [Organize the References, check the Language Quality]. After using this tool/service, the author(s) reviewed and edited the content as needed and take(s) full responsibility for the content of the published article.

Abbreviations

ABS	Acrylonitrile Butadiene Styrene
AFM	Atomic Force Microscopy
AM	Additive Manufacturing
ANN	Artificial Neural Network
ANOVA	Analysis of Variance
BF	Basalt Fibre
CAD	Computer-Aided Design
CCD	Central Composite Design
C_p	Specific Heat Capacity
DIC	Digital Image Correlation
DLP	Digital Light Processing
DMLS	Direct Metal Laser Sintering
DoE	Design of Experiment
DSC	Differential Scanning Calorimetry
DSD	Definitive Screening Design
FDM	Fused Deposition Modelling
FEA	Finite Element Analysis

FESEM	Field Emission Scanning Electron Microscopy
FFBPNN	Feedforward Backpropagation Neural Network
FFD	Fractional Factorial Design
FFF	Fused Filament Fabrication
FTIR	Fourier Transform Infrared Spectroscopy
GA	Genetic Algorithm
GRA	Gray Relational Analysis
k	Thermal Conductivity
L-PA	Low-Temperature Polyamide
ME	Material Extrusion
Micro CT	Microcomputed Tomography
ML	Machine Learning
PA-CF	Carbon Fibre-Reinforced Nylon
PAPC-II	Polyamide–Polyolefin–Cellulose Composite
PEEK	Polyether Ether Ketone
PEI	Polyetherimide
PETG	Polyethylene Terephthalate Glycol
PLA	Polylactic Acid
RBFNN	Radial Basis Function Neural Network
RSM	Response Surface Methodology
S/N	Signal-to-Noise
SAEA	Surrogate-Assisted Evolutionary Algorithm
SEM	Scanning Electron Microscopy
SLA	Stereolithography
SLJs	Single Lap Joints
SLS	Selective Laser Sintering
T_{cc}	Cold Crystallization Temperature
T_g	Glass Transition Temperature
T_m	Melting Temperature
UTS	Ultimate Tensile Strength
α	Coefficient of Thermal Expansion

References

1. He, F.; Thakur, V.K.; Khan, M. Evolution and new horizons in modelling crack mechanics of 3D printing polymeric structures. *Mater. Today Chem.* **2021**, *20*, 100393. [CrossRef]
2. Ergene, B.; İnci, Y.E.; Çetintaş, B.; Daysal, B. An experimental study on the wear performance of 3D printed polylactic acid and carbon fibre reinforced polylactic acid parts: Effect of infill rate and water absorption time. *Polym. Compos.* **2025**, *46*, 372–386. [CrossRef]
3. Kumar, A.; Dixit, A.R.; Sreenivasa, S. Mechanical properties of additively manufactured polymeric composites using sheet lamination technique and fused deposition modelling: A review. *Polym. Adv. Technol.* **2024**, *35*, e6396. [CrossRef]
4. Tofangchi, A.; Han, P.; Izquierdo, J.; Iyengar, A.; Hsu, K. Effect of ultrasonic vibration on interlayer adhesion in fused filament fabrication 3D printed abs. *Polymers* **2019**, *11*, 315. [CrossRef]
5. Gibson, I.; Rosen, D.; Stucker, B. *Additive Manufacturing Technologies: 3D Printing, Rapid Prototyping, and Direct Digital Manufacturing*, 2nd ed.; Springer: New York, NY, USA, 2015; pp. 1–498. [CrossRef]
6. Solomon, I.J.; Sevvel, P.; Gunasekaran, J. A review on the various processing parameters in fdm. *Mater. Today Proc.* **2020**, *37*, 509–514. [CrossRef]
7. Faes, M.; Ferraris, E.; Moens, D. Influence of inter-layer cooling time on the quasi-static properties of abs components produced via fused deposition modelling. *Procedia CIRP* **2016**, *42*, 748–753. [CrossRef]
8. Ahmad, M.; Javaid, M.; Haleem, A. A study on fused deposition modeling (fdm) and laser-based additive manufacturing (lbam) in the medical field. *Intell. Pharm.* **2024**, *2*, 381–391. [CrossRef]
9. Jamal, M.A.; Shah, O.R.; Ghafoor, U.; Qureshi, Y.; Bhutta, M.R. Additive manufacturing of continuous fiber-reinforced polymer composites via fused deposition modelling: A comprehensive review. *Polymers* **2024**, *16*, 1622. [CrossRef]
10. Acierno, D.; Patti, A. Fused deposition modelling (fdm) of thermoplastic-based filaments: Process and rheological properties—An overview. *Materials* **2023**, *16*, 7664. [CrossRef]

11. Shanmugam, V.; Babu, K.; Kannan, G.; Mensah, R.A.; Samantaray, S.K.; Das, O. The thermal properties of fdm printed polymeric materials: A review. *Polym. Degrad. Stab.* **2024**, *225*, 110902. [CrossRef]
12. Dey, A.; Yodo, N. A systematic survey of fdm process parameter optimization and their influence on part characteristics. *J. Manuf. Mater. Process.* **2019**, *3*, 64. [CrossRef]
13. Kumar, J.; Mishra, V.; Negi, S. An overview of research on fff based additive manufacturing of polymer composite. In *Recent Advancements in Mechanical Engineering*; ICRAMERD 2022, Lecture Notes in Mechanical Engineering; Springer: Singapore, 2022.
14. Jaisingh Sheoran, A.; Kumar, H. Fused deposition modeling process parameters optimization and effect on mechanical properties and part quality: Review and reflection on present research. *Mater. Today Proc.* **2020**, *21*, 1659–1672. [CrossRef]
15. Dizon, J.R.C.; Espera, A.H.; Chen, Q.; Advincula, R.C. Mechanical characterization of 3D-printed polymers. *Addit. Manuf.* **2018**, *20*, 44–67. [CrossRef]
16. Enyan, M.; Amu-Darko, J.N.O.; Issaka, E.; Abban, O.J. Advances in fused deposition modeling on process, process parameters, and multifaceted industrial application: A review. *J. Phys. Commun.* **2024**, *6*, 012401. [CrossRef]
17. Demir, S.; Yüksel, C. A comparative analysis of printing parameter effects of tensile and flexural specimens produced with two different printers by the taguchi method. *Prog. Addit. Manuf.* **2025**, *10*, 647–660. [CrossRef]
18. Vanaei, H.R.; Khelladi, S.; Deligant, M.; Shirinbayan, M.; Tcharkhtchi, A. Numerical prediction for temperature profile of parts manufactured using fused filament fabrication. *J. Manuf. Process.* **2022**, *76*, 548–558. [CrossRef]
19. Naveed, N. Investigating the material properties and microstructural changes of fused filament fabricated pla and tough-pla parts. *Polymers* **2021**, *13*, 1487. [CrossRef] [PubMed]
20. Wang, T.M.; Xi, J.T.; Jin, Y. A model research for prototype warp deformation in the fdm process. *Int. J. Adv. Manuf. Technol.* **2007**, *33*, 1087–1096. [CrossRef]
21. Kechagias, J.; Zaoutsos, S. Effects of 3D-printing processing parameters on fff parts' porosity: Outlook and trends. *Mater. Manuf. Process.* **2024**, *39*, 804–814. [CrossRef]
22. Yancy, C.K. Influence of Thermal Gradient on Mechanical Properties in Fused Deposition Modelling (FDM) Additive Manufacturing. Master's Thesis, A&M University, College Station, TX, USA, 2023.
23. Sun, Q.; Rizvi, G.M.; Bellehumeur, C.T.; Gu, P. Effect of processing conditions on the bonding quality of fdm polymer filaments. *Rapid Prototyp. J.* **2008**, *14*, 72–80. [CrossRef]
24. Lepoivre, A.; Boyard, N.; Levy, A.; Sobotka, V. Heat transfer and adhesion study for the fff additive manufacturing process. *Procedia Manuf.* **2020**, *47*, 948–955. [CrossRef]
25. Costa, S.F.; Duarte, F.M.; Covas, J.A. Thermal conditions affecting heat transfer in fdm/ffe: A contribution towards the numerical modelling of the process. *Virtual Phys. Prototyp.* **2015**, *10*, 35–46. [CrossRef]
26. Tsekmes, I.A.; Kochetov, R.; Morshuis, P.H.F.; Smit, J.J. Thermal conductivity of polymeric composites: A review. In Proceedings of the 2013 IEEE International Conference on Solid Dielectrics (ICSD), Bologna, Italy, 30 June–4 July 2013.
27. Gray, A.P. Polymer crystallinity determinations by dsc. *Thermochim. Acta* **1970**, *1*, 563–579. [CrossRef]
28. Ebewele, R.O. *Polymer Science and Technology*, 3rd ed.; CRC Press: Boca Raton, FL, USA, 2000; pp. 1–478.
29. Kanbur, B.B.; Markussen, W.B.; Duan, F.; Seat, M.H.; Kærn, M.R. Experimental indirect cooling performance analysis of the metal 3D-printed cold plates with two different supporting elements. *Int. Commun. Heat Mass Transf.* **2023**, *148*, 107046. [CrossRef]
30. Sinha, S.; Lynch, S.P.; Meisel, N.A. Heat transfer simulation of material extrusion additive manufacturing to predict weld strength between layers. *Addit. Manuf.* **2021**, *46*, 102117. [CrossRef]
31. Janna, W.S. *Engineering Heat Transfer*, 3rd ed.; CRC Press: Boca Raton, FL, USA, 2009; pp. 1–750.
32. Cosson, B.; Asséko, A.C.A.; Pelzer, L.; Hopmann, C. Radiative thermal effects in large scale additive manufacturing of polymers: Numerical and experimental investigations. *Materials* **2022**, *15*, 1052. [CrossRef]
33. Zhang, J.; Van Hooreweder, B.; Ferraris, E. T4f3: Temperature for fused filament fabrication. *Prog. Addit. Manuf.* **2022**, *7*, 971–991. [CrossRef]
34. Turner, B.N.; Strong, R.; Gold, S.A. A review of melt extrusion additive manufacturing processes: I. process design and modeling. *Rapid Prototyp. J.* **2014**, *20*, 192–204. [CrossRef]
35. Zhang, J.; Yang, T.; Jin, X.; Zheng, P.; Liu, Y.; Zhang, Z. Temperature analyses in fused filament fabrication: From filament entering the hot-end to the printed parts. *3D Print. Addit. Manuf.* **2022**, *9*, 132–142. [CrossRef] [PubMed]
36. Matsika-Klossa, C.; Chatzidai, N.; Kousiatza, C.; Karalekas, D. Characterization of thermal expansion coefficient of 3D printing polymeric materials using fiber bragg grating sensors. *Materials* **2024**, *17*, 4668. [CrossRef]
37. Rădulescu, B.; Postole, M.; Teodorescu-Drăghicescu, H.; Alexandru, H.; Constantin, G.; Răducanu, A.; Dănilă, M. Thermal expansion of plastics used for 3D printing. *Polymers* **2022**, *14*, 3061. [CrossRef]
38. Faust, J.L.; Kelly, P.G.; Jones, B.D.; Roy-Mayhew, J.D. Effects of coefficient of thermal expansion and moisture absorption on the dimensional accuracy of carbon-reinforced 3D printed parts. *Polymers* **2021**, *13*, 3637. [CrossRef] [PubMed]
39. Elhattab, K.; Bhaduri, S.B.; Sikder, P. Influence of fused deposition modelling nozzle temperature on the rheology and mechanical properties of 3D printed β-tricalcium phosphate (tcp)/polylactic acid (pla) composite. *Polymers* **2022**, *14*, 1222. [CrossRef]

40. Badiru, A.B.; Valencia, V.V.; Liu, D. *Additive Manufacturing Handbook: Product Development for the Defense Industry*, 3rd ed.; CRC Press: Boca Raton, FL, USA, 2017; pp. 1–600.
41. Rosli, A.A.; Shuib, R.K.; Ishak, K.M.K.; Hamid, Z.A.A.; Abdullah, M.K.; Rusli, A. Influence of bed temperature on warpage, shrinkage and density of various acrylonitrile butadiene styrene (abs) parts from fused deposition modelling (fdm). *AIP Conf. Proc.* **2020**, *2267*, 020072. [CrossRef]
42. Apaçoğlu-Turan, B.; Kırkköprü, K.; Çakan, M. Numerical modeling and analysis of transient and three-dimensional heat transfer in 3D printing via fused-deposition modeling (fdm). *Computation* **2024**, *12*, 27. [CrossRef]
43. Cozzolino, E.; Napolitano, F.; Papa, I.; Squillace, A.; Astarita, A. Influence of the heated-bed material on pla mechanical properties and energy consumption in the fdm process. *Arab. J. Sci. Eng.* **2025**, *50*, 2443–2453. [CrossRef]
44. Ansari, A.A.; Kamil, M. Effect of print speed and extrusion temperature on properties of 3D printed pla using fused deposition modeling process. *Mater. Today Proc.* **2021**, *45*, 5462–5468. [CrossRef]
45. Lee, C.Y.; Liu, C.Y. The influence of forced-air cooling on a 3D printed pla part manufactured by fused filament fabrication. *Addit. Manuf.* **2019**, *25*, 196–203. [CrossRef]
46. Nugroho, A.; Ardiansyah, R.; Rusita, L.; Larasati, I.L. Effect of layer thickness on flexural properties of pla (polylactid acid) by 3D printing. *J. Phys. Conf. Ser.* **2018**, *1130*, 012017. [CrossRef]
47. Armillotta, A.; Bellotti, M.; Cavallaro, M. Warpage of fdm parts: Experimental tests and analytic model. *Robot. Comput. Integr. Manuf.* **2018**, *50*, 140–152. [CrossRef]
48. Mwania, F.; Maringa, M.; Nsengimana, J.; van der Walt, J.G. Investigating surfaces, geometry and degree of fusion of tracks printed using fused deposition modelling to optimise process parameters for polymeric materials at meso-scale. *Rapid Prototyp. J.* **2024**, *30*, 159–172. [CrossRef]
49. Olleak, A.; Adcock, E.; Hinnebusch, S.; Dugast, F.; Rollett, A.D.; To, A.C. Understanding the role of geometry and inter-layer cooling time on microstructure variations in lpbf ti6al4v through part-scale scan-resolved thermal modeling. *Addit. Manuf. Lett.* **2024**, *9*, 100197. [CrossRef]
50. Benwood, C.; Anstey, A.; Andrzejewski, J.; Misra, M.; Mohanty, A.K. Improving the impact strength and heat resistance of 3D printed models: Structure, property, and processing correlationships during fused deposition modeling (fdm) of poly(lactic acid). *ACS Omega* **2018**, *3*, 4400–4411. [CrossRef]
51. Zhang, Y.; Chou, K. A parametric study of part distortions in fused deposition modelling using three-dimensional finite element analysis. *Proc. Inst. Mech. Eng. B J. Eng. Manuf.* **2008**, *222*, 959–967. [CrossRef]
52. Filipov, S.; Faragó, I. Implicit euler time discretization and fdm with newton method in nonlinear heat transfer modeling. *arXiv* **2018**, arXiv:1811.06337. [CrossRef]
53. Sun, Q.; Rizvi, G.M.; Bellehumeur, C.T.; Gu, P. Experimental study of the cooling characteristics of polymer filaments in fdm and impact on the mesostructures and properties of prototypes. In Proceedings of the 2003 International Solid Freeform Fabrication Symposium, Austin, TX, USA, 4–6 August 2003.
54. Pokluda, O.; Bellehumeur, C.T.; Vlachopoulos, J. Modification of frenkel's model for sintering. *AIChE J.* **1997**, *43*, 3253–3256. [CrossRef]
55. Bellehumeur, C.T.; Kontopoulou, M.; Vlachopoulos, J. The role of viscoelasticity in polymer sintering. *Rheol. Acta* **1998**, *37*, 270–278. [CrossRef]
56. Bellehumeur, C.; Li, L.; Sun, Q.; Gu, P. Modeling of Bond Formation Between Polymer Filaments in the Fused Deposition Modeling Process. *J. Manuf. Process.* **2004**, *6*, 170–178. [CrossRef]
57. Yang, F.; Pitchumani, R. Healing of thermoplastic polymers at an interface under nonisothermal conditions. *Macromolecules* **2002**, *35*, 3213–3224. [CrossRef]
58. Garzon-Hernandez, S.; Garcia-Gonzalez, D.; Jérusalem, A.; Arias, A. Design of FDM 3D Printed Polymers: An Experimental–Modelling Methodology for the Prediction of Mechanical Properties. *Mater. Des.* **2020**, *188*, 108414. [CrossRef]
59. Tymrak, B.M.; Kreiger, M.; Pearce, J.M. Mechanical Properties of Components Fabricated with Open-Source 3-D Printers under Realistic Environmental Conditions. *Mater. Des.* **2014**, *58*, 242–246. [CrossRef]
60. Rodríguez-Panes, A.; Claver, J.; Camacho, A.M. The Influence of Manufacturing Parameters on the Mechanical Behaviour of PLA and ABS Pieces Manufactured by FDM: A Comparative Analysis. *Materials* **2018**, *11*, 1333. [CrossRef]
61. Hamad, K.; Kaseem, M.; Deri, F. Melt Rheology of Poly (Lactic Acid)/Low Density Polyethylene Polymer Blends. *Adv. Chem. Eng. Sci.* **2011**, *1*, 208–214. [CrossRef]
62. Luzanin, O.; Movrin, D.; Stathopoulos, V.; Pandis, P.; Radusin, T.; Guduric, V. Impact of processing parameters on tensile strength, in-process crystallinity and mesostructure in fdm-fabricated pla specimens. *Rapid Prototyp. J.* **2019**, *25*, 1398–1410. [CrossRef]
63. Aloyaydi, B.A.; Sivasankaran, S.; Ammar, H.R. Influence of infill density on microstructure and flexural behavior of 3D printed pla thermoplastic parts processed by fusion deposition modeling. *AIMS Mater. Sci.* **2019**, *6*, 1033–1048. [CrossRef]
64. Tang, C.; Liu, J.; Yang, Y.; Liu, Y.; Jiang, S.; Hao, W. Effect of process parameters on mechanical properties of 3D printed pla lattice structures. *Compos. C Open Access* **2020**, *3*, 100076. [CrossRef]

65. Cardoso, P.H.M.; Coutinho, R.R.T.P.; Drummond, F.R.; Conceição, M.N.; Thiré, R.M.S.M. Evaluation of printing parameters on porosity and mechanical properties of 3D printed pla/pbat blend parts. *Macromol. Symp.* **2020**, *394*, 2000157. [CrossRef]
66. von Windheim, N.; Collinson, D.W.; Lau, T.; Brinson, L.C.; Gall, K. The influence of porosity, crystallinity and interlayer adhesion on the tensile strength of 3D printed polylactic acid (pla). *Rapid Prototyp. J.* **2021**, *27*, 1327–1336. [CrossRef]
67. Hikmat, M.; Rostam, S.; Ahmed, Y.M. Investigation of tensile property-based taguchi method of pla parts fabricated by fdm 3d printing technology. *Results Eng.* **2021**, *11*, 100264. [CrossRef]
68. Kamer, M.S.; Temiz, Ş.; Yaykaşlı, H.; Kaya, A.; Akay, O. Effect of printing speed on fdm 3D-printed pla samples produced using different two printers. *Int. J. 3D Print. Technol. Digit. Ind.* **2022**, *6*, 438–448. [CrossRef]
69. Auffray, L.; Gouge, P.A.; Hattali, L. Design of experiment analysis on tensile properties of pla samples produced by fused filament fabrication. *Int. J. Adv. Manuf. Technol.* **2022**, *118*, 4123–4137. [CrossRef]
70. Kumar, M.S.; Farooq, M.U.; Ross, N.S.; Yang, C.H.; Kavimani, V.; Adediran, A.A. Achieving effective interlayer bonding of pla parts during the material extrusion process with enhanced mechanical properties. *Sci. Rep.* **2023**, *13*, 6800. [CrossRef]
71. Ahmed, B.A.; Ahmed, E.S.; Elshaer, A.; Mekhemer, W.; Alsaleem, F.M.; Mohamed, O.A.; Serhatlı, U. Printing parameter optimization of additive manufactured pla using taguchi design of experiment. *Polymers* **2023**, *15*, 4370. [CrossRef] [PubMed]
72. Delbart, R.; Papasavvas, A.; Robert, C.; Truong Hoang, T.Q.; Martinez-Hergueta, F. An experimental and numerical study of the mechanical response of 3D printed pla/cb polymers. *Compos. Struct.* **2023**, *319*, 117156. [CrossRef]
73. Popović, M.; Pjević, M.; Milovanović, A.; Mladenović, G.; Milošević, M. Printing parameter optimization of pla material concerning geometrical accuracy and tensile properties relative to fdm process productivity. *J. Mech. Sci. Technol.* **2023**, *37*, 697–706. [CrossRef]
74. Wang, Z.; Wang, J.; Zhang, Y.; Li, Y.; Li, Y. Exploring the effects of processing parameters on the flexural performance of polylactic acid fabricated through a customized high extrusion rate fused filament fabrication system. *J. Mater. Eng. Perform.* **2024**, *33*, 14525–14537. [CrossRef]
75. Cadete, M.S.; Gomes, T.E.P.; Gonçalves, I.; Neto, V. Influence of 3D-printing deposition parameters on crystallinity and morphing properties of pla-based materials. *Prog. Addit. Manuf.* **2025**, *10*, 127–137. [CrossRef]
76. Gajjar, T.; Yang, R.; Ye, L.; Zhang, Y.X. Effects of key process parameters on tensile properties and inter-layer bonding behavior of 3D printed pla using fused filament fabrication. *Prog. Addit. Manuf.* **2025**, *10*, 1261–1280. [CrossRef]
77. Faizaan, M.; Baloor, S.S.; Nunna, S.; Mallya, R.; Udupi, S.R.; Kini, C.R.; Kada, S.R.; Creighton, C. A study on the overall variance and void architecture on mex-pla tensile properties through printing parameter optimisation. *Sci. Rep.* **2025**, *15*, 3103. [CrossRef]
78. Akhoundi, B.; Safi Jahanshahi, A. An experimental study on the influence of printing parameters on inter-raster bonding in a single-layer polylactic acid fabricated via fused filament fabrication. *J. Mater. Eng. Perform.* **2025**, *34*, 21270–21279. [CrossRef]
79. Kechagias, J.D.; Fountas, N.A.; Papantoniou, I.; Vaxevanidis, N.M. Interlaminar bonding assessment in vertical-oriented filament material extrusion bending specimens. *Int. J. Adv. Manuf. Technol.* **2025**, *136*, 4977–4989. [CrossRef]
80. Layeb, N.; Barhoumi, N.; Oldal, I.; Keppler, I. Improving the strength properties of pla acetabular liners by optimizing fdm 3D printing: Taguchi approach and finite element analysis validation. *Int. J. Adv. Manuf. Technol.* **2025**, *137*, 2649–2664. [CrossRef]
81. Hibbert, K.; Warner, G.; Brown, C.; Ajide, O.; Owolabi, G.; Azimi, A. The effects of build parameters and strain rate on the mechanical properties of fdm 3D-printed acrylonitrile butadiene styrene. *Open J. Org. Polym. Mater.* **2019**, *9*, 1–27. [CrossRef]
82. Srinivasan, R.; Pridhar, T.; Ramprasath, L.S.; Charan, N.S.; Ruban, W. Prediction of tensile strength in fdm printed abs parts using response surface methodology (rsm). *Mater. Today Proc.* **2020**, *27*, 1827–1832. [CrossRef]
83. Rachman, F.; Kurniawan, B.; Yoningtias, M. Optimization of 3D printing process parameters on tensile strength of abs filament material product using taguchi method. In Proceedings of the 4th International Conference on Applied Science and Technology on Engineering Science iCAST-ES, Samarinda, Indonesia, 23–24 October 2023; pp. 284–290. [CrossRef]
84. Nathaphan, S.; Trutassanawin, W. Effects of process parameters on compressive property of fdm with abs. *Rapid Prototyp. J.* **2021**, *27*, 905–917. [CrossRef]
85. Abbas, T.F.; Mansor, K.K.; Ali, H.B. The effect of fdm process parameters on the compressive property of abs prints. *J. Hunan Univ. Nat. Sci.* **2022**, *49*, 154–162. [CrossRef]
86. Ahmad, M.N.; Yahya, A. Effects of 3D printing parameters on mechanical properties of abs samples. *Designs* **2023**, *7*, 136. [CrossRef]
87. Yankin, A.; Alipov, Y.; Temirgali, A.; Serik, G.; Danenova, S.; Talamona, D.; Perveen, A. Optimization of printing parameters to enhance tensile properties of abs and nylon produced by fused filament fabrication. *Polymers* **2023**, *15*, 3043. [CrossRef] [PubMed]
88. Mushtaq, R.T.; Iqbal, A.; Wang, Y.; Rehman, M.; Petra, M.I. Investigation and optimization of effects of 3D printer process parameters on performance parameters. *Materials* **2023**, *16*, 3392. [CrossRef]
89. Khodaee, A.; Abedini, V.; Kami, A. Effects of fused filament fabrication (fff) process parameters on tensile and flexural properties of abs/pla multi-material. *J. Braz. Soc. Mech. Sci. Eng.* **2024**, *46*, 628. [CrossRef]
90. Ding, S.; Zou, B.; Wang, P.; Ding, H. Effects of nozzle temperature and building orientation on mechanical properties and microstructure of peek and pei printed by 3d-fdm. *Polym. Test.* **2019**, *78*, 105948. [CrossRef]

91. Kumar, M.A.; Khan, M.S.; Mishra, S.B. Effect of machine parameters on strength and hardness of fdm printed carbon fiber reinforced petg thermoplastics. *Mater. Today Proc.* **2020**, *27*, 975–983. [CrossRef]
92. Zhao, D.; Hart, C.; Weese, N.A.; Rankin, C.M.; Kuzma, J.; Day, J.B.; Salary, R. Experimental and computational analysis of the mechanical properties of biocompatible bone scaffolds fabricated using fused deposition modeling additive manufacturing process. In Proceedings of the ASME 2020 15th International Manufacturing Science and Engineering Conference, Virtual, 3 September 2020. [CrossRef]
93. Zhang, Y.; Mao, K.; Leigh, S.; Shah, A.; Chao, Z.; Ma, G. A parametric study of 3D printed polymer gears. *Int. J. Adv. Manuf. Technol.* **2020**, *107*, 4481–4492. [CrossRef]
94. Vaes, D.; Coppens, M.; Goderis, B.; Zoetelief, W.; Van Puyvelde, P. The extent of interlayer bond strength during fused filament fabrication of nylon copolymers: An interplay between thermal history and crystalline morphology. *Polymers* **2021**, *13*, 2677. [CrossRef]
95. Hsueh, M.-H.; Lai, C.-J.; Wang, S.-H.; Zeng, Y.-S.; Hsieh, C.-H.; Pan, C.-Y.; Huang, W.-C. Effect of printing parameters on the thermal and mechanical properties of 3D-printed pla and petg, using fused deposition modeling. *Polymers* **2021**, *13*, 1758. [CrossRef]
96. Vamshinath, K.; Kumar, N.N.; Kumar, R.T.; Nagaraju, D.S.; Sateesh, N.; Subbaiah, R. Analysis of the effect of the process parameters on the mechanical strength of 3D printed and adhesively bonded petg single lap joint. *Mater. Today Proc.* **2022**, *62*, 4509–4514. [CrossRef]
97. Sikder, P.; Challa, B.T.; Gummadi, S.K. A comprehensive analysis on the processing-structure-property relationships of fdm-based 3-d printed polyetheretherketone (peek) structures. *Materialia* **2022**, *22*, 101427. [CrossRef]
98. Padhy, C.; Simhambhatla, S.; Bhattacharjee, D. Ensembled surrogate assisted material extrusion based 3D printing process parameter optimization for enhanced mechanical properties of peek. *Res. Sq.* **2023**. [CrossRef]
99. Hua, L.; Wang, X.; Ding, L.; Zeng, S.; Liu, J.; Wu, Z. Effects of fabrication parameters on the mechanical properties of short basalt-fiber-reinforced thermoplastic composites for fused deposition modeling-based 3D printing. *Polym. Compos.* **2023**, *44*, 3341–3357. [CrossRef]
100. Gómez-Ortega, A.; Piedra, S.; Mondragón-Rodríguez, G.C.; Camacho, N. Dependence of the mechanical properties of nylon-carbon fiber composite on the fdm printing parameters. *Compos. A Appl. Sci. Manuf.* **2024**, *186*, 108419. [CrossRef]
101. Perez, D.B.; Celik, E.; Karkkainen, R.L. Investigation of Interlayer Interface Strength and Print Morphology Effects in FDM 3D-Printed PLA. *3D Print. Addit. Manuf.* **2021**, *8*, 23–32. [CrossRef]
102. Fu, Y.; Downey, A.; Yuan, L.; Pratt, A.; Balogun, Y. In situ monitoring for fused filament fabrication process: A review. *Addit. Manuf.* **2021**, *38*, 101749. [CrossRef]
103. Kishore, V.; Ajinjeru, C.; Nycz, A.; Post, B.; Lindahl, J.; Kunc, V.; Duty, C. Infrared Preheating to Improve Interlayer Strength of Big Area Additive Manufacturing (BAAM) Components. *Addit. Manuf.* **2017**, *14*, 7–12. [CrossRef]
104. Hossain, R.E.N.; Lewis, J.; Moore, A.L. In Situ Infrared Temperature Sensing for Real-Time Defect Detection in Additive Manufacturing. *Addit. Manuf.* **2021**, *47*, 102328. [CrossRef]
105. McBean, M.; Yi, N.; Chaplin, A.; Ghita, O. In-Process Thermal Monitoring of the Extrusion Additive Manufacturing Process with High Temperature Polymers. *Virtual Phys. Prototyp.* **2025**, *20*, e2555497. [CrossRef]
106. Baqasah, H.; He, F.; Zai, B.A.; Asif, M.; Khan, K.A.; Thakur, V.K.; Khan, M.A. In-situ dynamic response measurement for damage quantification of 3D-printed ABS cantilever beam under thermomechanical load. *Polymers* **2019**, *11*, 2079. [CrossRef]
107. Omer, M.A.E.; Shaban, I.A.; Mourad, A.-H.; Hegab, H. Advances in Interlayer Bonding in Fused Deposition Modelling: A Review. *Virtual Phys. Prototyp.* **2025**, *20*, e2522951. [CrossRef]
108. Khan, M.A.; Khan, S.Z.; Sohail, W.; Khan, H.; Sohaib, M.; Nisar, S. Mechanical fatigue in aluminium at elevated temperature and remaining life prediction based on natural frequency evolution. *Fatigue Fract. Eng. Mater. Struct.* **2015**, *38*, 897–903. [CrossRef]
109. Doğanay Kati, H.; He, F.; Khan, M.; Gökdağ, H.; Alshammari, Y.L.A. Effect of printing parameters on the dynamic characteristics of additively manufactured abs beams: An experimental modal analysis and response surface methodology. *Polymers* **2025**, *17*, 1615. [CrossRef]
110. He, F.; Ning, H.; Khan, M. Effect of 3D printing process parameters on damping characteristic of cantilever beams fabricated using material extrusion. *Polymers* **2023**, *15*, 257. [CrossRef]
111. He, F.; Khan, M. Effects of printing parameters on the fatigue behaviour of 3D-printed abs under dynamic thermo-mechanical loads. *Polymers* **2021**, *13*, 2362. [CrossRef] [PubMed]
112. Tian, Y.; Zheng, B.; Khan, M.; He, F. Influence of sliding direction relative to layer orientation on tribological performance, noise, and stability in 3D-printed abs components. *Tribol. Int.* **2025**, *210*, 110762. [CrossRef]
113. Abusabir, A.; Khan, M.A.; Asif, M.; Khan, K.A. Effect of Architected Structural Members on the Viscoelastic Response of 3D Printed Simple Cubic Lattice Structures. *Polymers* **2022**, *14*, 618. [CrossRef] [PubMed]

114. Zhang, P.; He, F.; Khan, M. Optimization of printing parameters for self-lubricating polymeric materials fabricated via fused deposition modelling. *Polymers* **2025**, *17*, 1401. [CrossRef]
115. He, F.; Khan, M.; Aldosari, S. Interdependencies between dynamic response and crack growth in a 3D-printed acrylonitrile butadiene styrene (abs) cantilever beam under thermo-mechanical loads. *Polymers* **2022**, *14*, 982. [CrossRef]

Disclaimer/Publisher's Note: The statements, opinions and data contained in all publications are solely those of the individual author(s) and contributor(s) and not of MDPI and/or the editor(s). MDPI and/or the editor(s) disclaim responsibility for any injury to people or property resulting from any ideas, methods, instructions or products referred to in the content.



https://dspace.org/

Fundamentals of cooling rate and Its thermodynamic interactions in material extrusion

Alzahrani, Ahmad Saeed; Khan, Muhammad; He, Feiyang

2025-12-01
MDPI
https://doi.org/10.3390/jmmp9120412
Alzahrani AS, Khan M, He F. (2025) Fundamentals of cooling rate and its thermodynamic interactions in material extrusion. Journal of Manufacturing and Materials Processing, Volume 9, Issue 12, December 2025, Article number 412.

Downloaded from a DSpace repository. https://dspace.org/